NASA TECHNICAL MEMORANDUM

NASA TM X-62,012

NASA TM X-62,012

ELECTRICAL CONDUCTIVITY AND TEMPERATURE OF THE LUNAR INTERIOR FROM MAGNETIC TRANSIENT RESPONSE MEASUREMENTS

by Palmer Dyal, Curtis W. Parkin, Charles P. Sonett, and David S. Colburn

Ames Research Center
Moffett Field, Calif. 94035
December 1970

Electrical Conductivity and Temperature of the Lunar Interior from Magnetic Transient-Response Measurements

Palmer Dyal, Curtis W. Parkin, Charles P. Sonett,

and David S. Colburn

Ames Research Center, Moffett Field, Calif. 94035

ABSTRACT

The response of the moon to magnetic-field step transients in the solar wind has been investigated for seventy-five events, using simultaneous data from the Apollo 12 lunar surface magnetometer and the lunar orbiting Explorer 35 magnetometer. These transient events were all selected at times when the moon was in the free-streaming solar wind and the Apollo 12 magnetometer was on the lunar dark side. The lunar-nighttime Apollo 12 magnetometer data consistently show a distinct difference between radial and tangential surface magnetic-field components for all step transients; this property strongly implies that the surface magnetometer is measuring a global rather than a local effect. The simplest model which qualitatively explains all the general aspects of the dark-side transient-response data is a spherically symmetric three-layer model having a thin outer crust of very low electrical conductivity. The intermediate layer, of radial thickness $R_1 - R_2$, where $0.95R_{moon} \leq R_1 < R_{moon}$ and $R_2 \leq 0.6R_{moon}$, has an electrical conductivity $\sigma_1 = 1.7 \pm 0.4 \times 10^{-4}$ mhos/meter; the inner core has a maximum radius $R_2 \sim 0.6R_{moon}$ and minimum conductivity $\sigma_2 \sim 10^{-2}$ mhos/meter. Temperatures are calculated from these conductivities for several possible

lunar material compositions. For the example of an olivine moon, the temperatures of the layers are as follows: crust, ≤ 530° K; intermediate layer, 840° K; core, ≥ 1240° K.

INTRODUCTION

Astronauts Conrad and Bean set up the first magnetic observatory on the moon during the lunar surface exploration phase of the Apollo 12 mission. This magnetometer is one of the five scientific instruments collectively called the Apollo Lunar Surface Experiments Package (ALSEP). It measures three components of the vector magnetic field every 0.3019 second in the range 0 to 400 gammas with a resolution of 0.2 gamma and transmits this data to earth, where it is recorded continuously during the one-year ALSEP mission. The magnetometer is located at 23.35° west longitude and 2.97° south latitude in selenographic coordinates and lies 265 meters from the Surveyor III spacecraft [*Holt and Rennilson*, 1970]. The primary purpose of this magnetometer experiment is to measure the surface magnetic field and to investigate the electrical properties deep in the lunar interior. A secondary objective is to study the interaction of the moon with the solar wind. Measurements of the ambient driving magnetic field taken simultaneously at the lunar orbiting Explorer 35 satellite [*Sonett et al.*, 1967a] are used to determine the ambient field which surrounds the moon and also to describe the time-dependent fields which induce eddy currents inside the moon.

The electromagnetic environment at the moon varies strongly with the lunar spatial position during each orbit around the earth (see Figure 1). During full moon the magnetic-field environment is governed by the earth's dipolar field (which averages ~10γ at the lunar position)

Fig. 1

and the neutral sheet in the geomagnetic tail which separates the inward- and outward-directed field components. Prior to and subsequent to full moon, the moon traverses the magnetosheath, a region of shocked plasma and turbulent magnetic fields (averaging ~8γ at the moon) which is produced by the interaction of the earth's magnetic dipole field with the solar plasma emanating from the sun. Outside the magnetosheath region, the moon is immersed in the direct solar wind and a frozen-in solar field of ~5γ. The electromagnetic properties of each of these three main spatial regions are distinct and cause different responses by the moon.

During the last decade, considerable progress was made toward determination of the electromagnetic properties of the moon. The first magnetic-field measurements near the moon were made by the USSR space probe Luna 2 [*Dolginov et al.*, 1961]. The lunar field was found to have an upper limit of 50 gammas at an altitude of 55 km from the surface. Further measurements were made by the lunar orbiting USSR satellite Luna 10 which approached to within 350 km of the lunar surface. From analysis of these data *Dolginov et al.* [1966] reported a 15-gamma magnetic field associated with a lunar magnetosphere. *Sonett et al.* [1967a] and *Ness et al.* [1967] measured the magnetic field onboard the lunar orbiting spacecraft Explorer 35 and set an upper limit of 2 gammas for an intrinsic lunar field at satellite periselene (800 km above the surface). This placed an upper limit of 7 gammas for a permanent global field at the surface and set the magnetic moment upper bound at 6×10^{20} gauss-cm^3 for an assumed centered lunar magnetic dipole. Later analysis by *Behannon* [1968] set this upper bound at 10^{20} gauss-cm^3.

Actual magnetic measurements of lunar surface samples have been completed at many laboratories. Remanent magnetization of Apollo 11 samples

was found to lie generally in the range 10^{-3} to 10^{-5} emu/g [see, e.g., *Doell et al.*, 1970; *Strangway et al.*, 1970; *Runcorn et al.*, 1970].

Using Explorer 35 measurements obtained on both sides of the neutral sheet in the geomagnetic tail, *Behannon* [1968] determined the bulk relative permeability of the moon to be less than 1.8. Experiments on Surveyors V and VI showed that lunar soil at those sites contain less than 1% ferrous magnetic material by volume [*de Wys*, 1968]; if the magnetic material is assumed to be magnetite, the relative permeability of the surface material at those sites is 1.04. Direct magnetic susceptibility measurements of samples from the Apollo 11 site [*Nagata et al.*, 1970; *Strangway et al.*, 1970; *Runcorn et al.*, 1970; *Larochelle and Schwarz*, 1970] indicate permeabilities ranging from 1.0006 to 1.08 for lunar surface materials.

The relative dielectric constant of the lunar surface material has been measured by earth- and satellite-based radar experiments. *Hagfors* [1966], in his review of earth-based observations of the moon, showed that a relative dielectric constant of 2.6 is consistent with backscattered measurements at 10^8 Hz. *Brown et al.* [1967] calculated a value of 3.5 ± 0.7 at 10^{10} Hz by using data from the radar altimeter and the Doppler velocity sensor of the Surveyor III spacecraft. Returned Apollo 11 samples were found to have dielectric constants ranging from 6 to 15 at 10^8 Hz [*Chung et al.*, 1970].

Calculations from lunar orbiting satellite magnetometer data have yielded upper limits for the bulk lunar electrical conductivity, while returned samples have allowed direct measurements of conductivities of lunar surface material. *Colburn et al.* [1967], using the Explorer 35

magnetometer measurements, estimated the conductivity to be less than 10^{-6} mhos/meter for a homogenous moon. They also stated that the measurements were consistent with a core of higher conductivity surrounded by a surface shell of very low conductivity. *Ness* [1968], from similar measurements on the satellite, concluded that the effective homogenous lunar conductivity is less than 10^{-5} mhos/meter. In a later paper on the eddy-current response, *Ness* [1969] calculated a core conductivity of 8×10^{-5} mhos/meter for a lunar model with a homogenous core of radius 1350 km surrounded by a nonconducting crust. He used simultaneous measurements from Explorer 33 and Explorer 35 to analyze the lunar response to a solar-wind magnetic discontinuity. Nonhomogeneous lunar conductivity models have been considered by other investigators [e.g., *England et al.*, 1968; *Ward*, 1969; *Hollweg*, 1970]. Measurements by *Nagata* [1970] and *Chung et al.* [1970] showed that the Apollo 11 surface material at room temperature in the laboratory possesses a direct-current conductivity in the range 10^{-7} to 10^{-9} mhos/meter.

Theoretical studies of the electrodynamic response of the moon to time-dependent solar-wind fields have been completed by many authors. Two types of whole-moon magnetic induction fields are treated: a poloidal field due to eddy currents driven by time-varying external magnetic fields, and a toroidal field due to unipolar currents driven through the moon by the motional solar-wind $\vec{V} \times \vec{B}$ electric field.

In the poloidal case, eddy currents are induced in the moon by the changes in the external magnetic field; associated with these currents is a poloidal lunar magnetic field which tends to oppose the changes in the driving field (see Figure 2a). The lunar poloidal response has been

Fig. 2

treated by *Gold* [1966] and *Tozer and Wilson* [1967], who assumed that the interaction with the solar wind could be characterized by a Cowling time constant $\mu\sigma R_m^2$, where R_m is the radius of the moon, μ the permeability, and σ the electric conductivity. Gold postulated that the time constant would be long compared to a lunar rotation period and that the magnetic-field lines would pile up on the front side and produce a shock wave. Magnetometers and plasma probes onboard Explorer 35 did not detect this shock wave. The classical eddy-current response of a homogenous sphere to alternating and transient magnetic fields in a vacuum has been described by *Smythe* [1950] and by *Wait* [1951]. The case where the sphere is immersed in a plasma rather than a vacuum is a much more complicated problem. *Schubert and Schwartz* [1969] and *Sill and Blank* [1970] have considered the overall time-dependent response of the moon to a fluctuating solar-wind field. By assuming simplifying boundary conditions, one can solve the vector Helmholtz equation for the time-dependent lunar field induced by the time-varying magnetic field and the motional electrical field in the solar wind. These solutions allow one to determine the electrical conductivity profile of the lunar interior if given the magnetic field at the lunar surface and the external driving field as functions of frequency.

In the toroidal case, first treated by *Sonett and Colburn* [1967], a unipolar steady-state current is generated in the moon and closes in the solar plasma. This current is driven by an electric field $\vec{E} = \vec{V} \times \vec{B}$, produced as the solar magnetic field $\vec{B}$, frozen in the solar plasma, sweeps by the moon with a relative velocity $\vec{V}$. The current driven by this electric field will distort the magnetic field as it diffuses into the lunar interior. The current system induces a toroidal magnetic field

with a magnitude inversely proportional to the total resistance to current flow through the moon (see Figure 2b). The unipolar current magnitude is limited by the region of lowest conductivity in the current path, whereas the eddy current magnitude is not. Even a very thin crust of low conductivity, therefore, can effectively quench the toroidal mode, allowing the poloidal response to dominate.

The induced lunar poloidal and toroidal fields can be studied by analysis of simultaneous measurements by magnetometers on the lunar surface and in the space surrounding the moon. In this paper we examine the response of the moon to a magnetic step transient (e.g., a tangential discontinuity) in the solar wind. The Apollo 12 magnetometer measures the vector sum of the lunar response field and the external driving field at the surface, while the Explorer 35 magnetometer, when positioned in the free-streaming solar wind, measures the driving field alone. The time-dependent decay characteristics of the induced fields are dependent upon the interior electrical conductivity, permitting a lunar electrical conductivity profile to be calculated from the time-series response measurements. Furthermore, since the conductivity is a known function of temperature [*Rikitake*, 1966], we calculate temperature profiles of the lunar interior for assumed material compositions of the moon.

EXPERIMENTAL TECHNIQUE

In this experiment the response of the moon to a magnetic transient is investigated by measuring the magnetic field simultaneously at the lunar surface and in the free-streaming solar wind near the moon. The surface magnetometer measures the vector sum of the driving and response

fields while the distant orbiting magnetometer measures only the input driving field as a function of time.

The Apollo 12 lunar surface magnetometer was activated by Astronauts Conrad and Bean at 1439 hours GMT, 19 November 1969, and it continuously transmits magnetic-field data from the lunar surface. Other instruments deployed by the astronauts include a passive seismometer, a solar-wind experiment, a suprathermal ion detector, and a cold-cathode pressure gauge. These instruments, along with a central-station radio receiver-transmitter and a nuclear power source, are designed to measure lunar parameters continuously for a period of one year. The magnetometer developed for the Apollo 12 mission is shown in Figure 3, and the critical instrument properties are listed in Table 1. (See *Dyal et al.* [1970b] for a detailed description of the instrument.)

Fig. 3

Apollo 12 magnetometer sensors and sensor orientations. Three orthogonal vector components of the magnetic field are measured by three fluxgate sensors. The theory of operation for the fluxgate sensors has been described in detail by *Geyger* [1964] and *Gordon et al.* [1965]. The fluxgate sensors, located at the ends of three 100-cm-long orthogonal booms, are separated from each other by 150 cm and are 75 cm above the ground. Prelaunch test results show that the 100-cm separation of the sensors from the magnetometer electronics and the 15-m separation between the sensors and other Apollo 12 instruments limit the magnetic field due to artificial sources to less than 0.2 gamma at the sensor locations.

The Apollo 12 magnetometer is deployed on the lunar surface so that each sensor is directed approximately 35° above the horizontal. The Z-sensor is pointed toward the east, the X-sensor toward the northwest, and the Y-sensor completes a right-hand orthogonal system. Figure 3 is a

photograph taken by Astronaut Bean of the magnetometer and Astronaut Conrad aligning the telemetry antenna toward earth.

Orientation measurements with respect to lunar coordinates are made with two devices. A shadowgraph is used by the astronaut to align and measure the azimuthal orientation with respect to the moon-to-sun line to an accuracy of 0.5°. The orientation in two orthogonal vertical planes is measured with gravity-level sensors which measure the tilt angle to an accuracy of 0.2° every 4.8 seconds. Orientation has remained relatively level, to within 3.2° of vertical, during the first 8 months of operation. There is a periodic shift of ±0.5° which corresponds to the lunar day-night cycle, and the instrument has slowly tilted in one direction by 0.5° during the first 8 months.

Each of the three fluxgate sensors can be oriented in three mutually orthogonal directions by three motors driven by the site-survey and flip-calibrate electronic sequencers. These digital sequencers are started by ground command or internally generated central-station commands. The sensor orientation is measured and transmitted to earth every 9.6 seconds. During the site-survey or gradient mode of operation the sensors are flipped and rotated in order to measure, simultaneously at all three sensors, each of the three orthogonal components of the magnetic field. This permits the gradient to be calculated in the plane of the sensors. During a flip-calibration mode of operation, four sets of amplitude calibration fields are generated for sensor calibration and a toggle is used to rotate the sensors 180° to determine the sensor zero offset.

Internal data processing. Internal data processing of the magnetic-field measurements requires the major portion of the magnetometer electronics. The sensor electronics has three operating ranges at ±100γ, ±200γ,

or ±400γ, any of which can be selected by ground command. Calibration and DC offset fields are generated by producing precisely known currents in the sensor feedback windings. The analog output of the sensor electronics is internally processed by a low-pass prealias filter, an analog-to-digital converter, a low-pass digital filter, and a telemetry encoder; the output is transmitted to earth via the central-station S-band transmitter. These filters and data samples are designed to provide the maximum amount of data for available telemetry bit rate. Hardware limitations require the filter cutoff frequency to be much less than half the sampling frequency, as dictated by the Nyquist sampling theorem.

The magnetometer has two data samplers: the analog-to-digital converter (26.5 samples/second) and the central-station telemetry encoder (3.3 samples/second). The prealias filter following the sensor electronics has attenuations of 3 db at 1.7 Hz, 64 db at 26.5 Hz, and 58 db at the Nyquist frequency (13.2 Hz), with an attenuation rate of 22 db/octave. The four-pole Bessel digital filter limits the alias error to less than 0.05% and has less than 1% overshoot for a step-function response. This filter has an attenuation of 3 db at 0.3 Hz and 48 db at the telemetry-sampling Nyquist frequency (1.6 Hz) and has phase response that is linear with frequency. The digital filter can be bypassed by ground command in order to pass higher frequency information with a possible corresponding increase in aliasing error.

The magnetometer experiment is controlled from the Manned Spacecraft Center, Houston, Texas, by commands transmitted from remote tracking stations. There are ten ground commands and one internal spacecraft command which establish the desired operational mode of the instrument. The digital data is recorded on magnetic tapes at the remote sites and sent to Ames Research Center for analysis.

Explorer 35 magnetometer. The ambient steady-state and time-dependent fluctuating magnetic fields in the lunar environment are measured by the Explorer 35 satellite magnetometer. A typical Explorer 35 orbit during a period when the Apollo 12 magnetometer was on the lunar dark side and the moon was immersed in the solar wind is shown in Figure 4. Fig. 4 The satellite has an orbital period of 11.5 hours, aposelene of 9390 km, and periselene of 2570 km. The Explorer 35 magnetometer measures three magnetic-field vector components every 6.14 seconds and has an alias filter with 18-db attenuation at the Nyquist frequency (0.08 Hz) of the spacecraft data-sampling system. For further information on this magnetometer, see *Sonett et al.* [1967b].

TRANSIENT MAGNETIC-FIELD MEASUREMENTS AND ANALYSIS

Seventy-five step-function transients which have penetrated the moon have been measured and analyzed using simultaneous data from the Apollo 12 lunar surface magnetometer and the lunar orbiting Explorer 35 magnetometer. These are the first measurements which clearly show a whole-moon spherical response to magnetic-field transients in interplanetary space.

These transients were selected from time periods when the moon was in the free-streaming solar wind and the surface magnetometer was on the lunar dark side. During these times the sunlit hemisphere of the moon obstructs the solar-wind flow, forming an elongated cavity which extends downstream for several lunar radii [*Colburn et al.*, 1967; *Lyon et al.*, 1967; *Ness et al.*, 1968]. Compared to the free-streaming solar wind, the plasma density on the dark-side surface is lower by two orders of magnitude [*Snyder et al.*, 1970] and is down by at least one order of magnitude in the cavity [*Serbu*, 1969].

The poloidal magnetic field induced in the moon by transients in the solar wind extend out into this cavity and can be measured at the lunar surface (see Figure 2a). In this paper, the distortion of the poloidal field lines due to compressive effects on the sunlit side and to the effects of solar-wind hydrodynamic flow past the moon [*Michel*, 1968; *Whang*, 1968; *Spreiter et al.*, 1970] will be neglected to a first approximation for measurements made on the dark-side surface. The justification for this approximation will be discussed in a subsequent paragraph.

A first overall scan of the Apollo 12 data revealed that the dark-side transient measurements show a remarkable similarity to the response of a conducting sphere in a vacuum. Measured surface magnetic-field radial components show a characteristic damped response to solar-wind field step transients, while components tangent to the lunar sphere show rapid response and overshoot initially, followed by decay to a steady-state value. The characteristics of these transient measurements suggest the use of a simple two-layer model of the moon as a first approximation.

Two-layer model and theory. An insert of Figure 5 schematically shows this two-layer model, which has the following assumed properties: The spherically symmetric model has a homogeneous inner core of scalar electrical conductivity σ_1 and radius R_1 surrounded by a nonconducting outer shell of outer radius R_m (the lunar radius). The sphere is in a vacuum and permeability is everywhere that of free space ($\mu = \mu_o$). Conduction currents dominate displacement currents within the sphere and dimensions of external field transients are large compared to the diameter of the sphere. The toroidal induction mode is assumed to be negligible compared to the poloidal mode. The validity and limitations of these

Fig. 5

assumptions will become apparent in the fit of the data to the model and will be discussed in subsequent paragraphs. Using these assumptions, the magnetic-field solutions of Maxwell's equations for the two-layer model is derived in the appendix.

The coordinate systems used for this model are shown in Figure 5. Total magnetic fields measured at the surface of the sphere are noted by the subscript A (corresponding to Apollo 12 lunar surface magnetometer measurements: $\vec{B}_A$) and external applied magnetic fields are noted by the subscript E (corresponding to lunar orbiting Explorer 35 magnetometer measurements: $\vec{B}_E$). The orthogonal unit vectors ($\hat{r}$, $\hat{\theta}$,$\hat{\phi}$) form a spherical system; the external field step-change vector ($\overrightarrow{\Delta B_E}$) and the radius vector to the Apollo 12 site lie in the $\hat{r}$ - $\hat{\theta}$ plane. All data are expressed in a surface coordinate system ($\hat{x}$, $\hat{y}$, $\hat{z}$) which has its origin at the Apollo 12 magnetometer site; $\hat{x}$ is directed radially outward from the surface, while $\hat{y}$ and $\hat{z}$ are tangent to the surface, directed eastward and northward, respectively.

Solutions of Maxwell's equations for the vector components of the magnetic field at the lunar surface are listed below for the case of an external magnetic-field step transient of magnitude $\overrightarrow{\Delta B_E} = \vec{B}_{Ef} - \vec{B}_{Eo}$ applied to the lunar sphere at time $t = 0$; $\vec{B}_{Eo}$ and $\vec{B}_{Ef}$ are Explorer 35 initial and final external fields, respectively. For $t < 0$, the magnetic-field vector components at the lunar surface ($\vec{B}_A$ measured by the Apollo 12 magnetometer) and corresponding pretransient field components in the space surrounding the moon ($\vec{B}_E$ measured by Explorer 35) are identical:

$t < 0$:

$$B_{Ax} = B_{Exo} \tag{1}$$

$$B_{Ay} = B_{Eyo} \tag{2}$$

$$B_{Az} = B_{Ezo} \tag{3}$$

For times after the arrival of the step transient, the solutions for the components of the vector field measured on the lunar surface can be expressed as follows:

$t > 0$:

$$B_{Ax} = -3\left(\frac{R_1}{R_m}\right)^3 (\Delta B_{Ex})F(t) + B_{Exf} \tag{4}$$

$$B_{Ay} = \frac{3}{2}\left(\frac{R_1}{R_m}\right)^3 (\Delta B_{Ey})F(t) + B_{Eyf} \tag{5}$$

$$B_{Az} = \frac{3}{2}\left(\frac{R_1}{R_m}\right)^3 (\Delta B_{Ez})F(t) + B_{Ezf} \tag{6}$$

where

$$\Delta B_{Ei} = B_{Eif} - B_{Eio}, \quad i = x, y, z. \tag{7}$$

Here R_1 and R_m are radii of the conducting core and the moon, respectively. B_{Eio} and B_{Eif} are the initial and final external applied field components, respectively, and are both measured by Explorer 35. B_{Ai} are total surface fields measured by the Apollo 12 magnetometer, and the time-dependence of the magnetic field is expressed as

$$F(t) = \frac{2}{\pi^2} \sum_{s=1}^{\infty} \frac{1}{s^2} \exp\left(\frac{-s^2\pi^2 t}{\mu_o \sigma_1 R_1^2}\right). \tag{8}$$

The function $F(t)$ is plotted versus $t/\mu_o\sigma_1 R_1^2$ in Figure 6, and it is easily seen that the series converges to zero for $t \to \infty$. See the appendix for a detailed derivation of equations (1) through (8). Fig. 6

Solutions (4), (5), and (6) for radial and tangential transients are shown in Figure 7. The various curves B_{Ai} in Figures 7b and 7c represent the components of the total magnetic field at the lunar surface; this total field is the vector sum of the applied solar field (Figure 7a) and the poloidal lunar eddy-current induced field. At the time of the transient ($t = 0$), eddy currents are established in the conductor which oppose Fig. 7

diffusion of the external magnetic field into the sphere. For times $t > 0$, the eddy currents decay and the external field diffuses into the conductor.

Figure 7b shows the response to both rising and falling step transients in the radial component of the external field. All radial response curves (B_{Ax}) show a characteristic damped appearance since the radial component of the eddy-current field always opposes the radial component of the external field. The initial ($t = 0$) value of the total surface field is determined by the size of the conducting core relative to that of the whole moon, i.e., by $(R_1/R_m)^3$. For $t > 0$, the eddy-current field decays in a roughly exponential fashion (see equation (8) and Figure 6), causing the total surface field to approach asymptotically the post-transient value of the external field. The rate of decay is dependent on the conductivity σ_1 and radius R_1 of the conducting sphere.

The surface tangential response to both rising and falling step transients is shown in Figure 7c. The tangential components of the eddy-current induced field are always of the same polarity as the tangential components of the external field; this causes characteristic overshoot in all B_{Ay} and B_{Az} curves, quite in contrast to the appearance of the radial component B_{Ax}. Again the initial ($t = 0$) value of the total surface field is determined by the relative size factor $(R_1/R_m)^3$. The initial overshoot magnitude is limited to the maximum value $\Delta B_{Ey}/2$ or $\Delta B_{Ez}/2$ for the case $R_1 \to R_m$. For $t > 0$, the tangential component of the surface field decays to the post-transient value of the external field tangential component, again according to equation (8).

Comparison of the data to the two-layer model. The general appearance of the seventy-five transients studied was similar to the theoretical curves

shown in Figure 7. Several examples will be examined to show this qualitative agreement. For all data the Apollo 12 and Explorer 35 scales differ since the 36 ± 5 gamma steady field at the surface site [*Dyal et al.*, 1970a] has been retained in the Apollo 12 data.

A typical step-function transient involving all three vector components is shown in Figure 8. One can easily see the characteristic damped decay in the Apollo radial data (B_{Ax}) and overshoot in the tangential data (B_{Ay} and B_{Az}). One can also see from the external field magnitude $|\vec{B}_E|$ curve that this transient is a tangential discontinuity involving primarily a field direction change. This external field direction change does, however, produce a step change in the Apollo 12 magnitude $|\vec{B}_A|$ curve since it vectorally adds to the local steady field at the Apollo 12 site.

Fig. 8

Figure 9 shows a clear example of radial response to four sequential transients, approximately two minutes apart. The damped response of the B_{Ax} component, directed radially outward from the moon, is exceptionally distinct. This particular transient also involved only a field direction change and not a magnitude change, as indicated by the magnitude plot $|\vec{B}_E|$ of the Explorer 35 data.

Fig. 9

Figure 10 shows a transient which is tangent to the lunar sphere in the Y (easterly) direction. One can clearly see the overshoot in the Apollo 12 y-component (B_{Ay}) in response to the transient in the Explorer 35 y-component (B_{Ey}). Thereafter the induced eddy currents diminish and the total surface field B_{Ay} approaches the post-transient exterior-field value (B_{Eyf}).

Fig. 10

All transient measurements exhibit characteristic damping in the surface field radial component and overshoot in the tangential component. The

distinct difference between radial and tangential measurements clearly shows symmetry with respect to the lunar sphere; this strongly implies that the transient response is a whole-moon effect and discounts the possibility that the measured induction fields are due to a smaller conducting body set off to one side of the Apollo 12 magnetometer.

The theoretical $F(t)$ function given in equation (8) has been fitted by the least-squares method to the post-transient ($t > 0$) Apollo 12 measurements over four-minite intervals. A theory-to-data least-squares fit for one particular transient is shown in Figure 11. For this transient, values of $\sigma_1 = 1.5 \times 10^{-4}$ mhos/meter and $0.95R_m \leq R_1 < R_m$ best fit the data. Dashed curves in Figure 11 show the strong dependence of $F(t)$ on the electrical conductivity σ_1 for values of σ_1 varying from 1.5×10^{-4} by factors of 0.1, 0.5, 2, and 10. The average value of the electrical conductivity for ten transient events was calculated to be $1.7 \pm 0.4 \times 10^{-4}$ mhos/meter.

Fig. 11

A determination of the radius of the conducting core was made by comparing the features at the start of the rise or fall portion of the response curves (as shown in Figure 7) with the data. The transients in the radial component indicate that the instrument is relatively close to the conducting core. By comparison with theoretical curves, the conducting-core radius was calculated to be in the range $0.95R_m \leq R_1 < R_m$. For these average calculated values of σ_1 and R_1, the theoretical time-dependent function $F(t)$ of equation (8) will decay to less than 2% of its initial value within four minutes.

Deviations from the two-layer model and introduction of a three-layer model. Examination of the time series step response for periods longer

than four minutes revealed that the data deviates slightly from the two-layer model. In particular, the total surface field measured by Apollo 12 does not decay exactly to the Explorer 35 final field value within this four-minute time period for either radial or tangential components.

In order to investigate this deviation, differences between field component values measured at $t = 0$ and at $t = +4$ minutes in the Apollo 12 data were plotted against corresponding differences in the Explorer 35 data. These plots, ΔB_{Ai} vs. ΔB_{Ei}, appear in Figure 12. Each point corresponds to a separate transient event occurring when the Apollo 12 magnetometer was on the lunar dark side. A reference line of slope one is shown on each plot, indicating the functional dependence of ΔB_{Ai} on ΔB_{Ei} for a two-layer model which decays to an asymptotic value within four minutes. It is seen that for the radial component the slope of a least-squares straight line to the data is ~0.8, i.e., Apollo 12 lunar surface fields, in general, fall short of the Explorer 35 asymptotes by about 20% after four minutes. For tangential components, on the other hand, the least-squares slope is ~1.35, indicating that the Apollo 12 data fails to decay back to the final Explorer 35 asymptote by about 35% after the initial overshoot.

Fig. 12

Another characteristic of these field differences is that the ratios $\Delta B_{Ai}/\Delta B_{Ei}$, obtained at times ranging from sunset to past midnight, are independent of the distance of the magnetometer from the solar-wind cavity boundary. This, in turn, implies that the deviation from the two-layer model is not a function of position in the lunar cavity, and therefore effects of solar-wind hydrodynamic flow past the moon can be neglected.

In order to investigate the departure from two-layer theory, three possible conditions that were excluded in the assumptions of the two-layer model are qualitatively re-examined here: (1) the existence of a shell of

permeability several times greater than μ_o in the moon, (2) a toroidal induction mode large enough to be measured, and (3) a deep core of conductivity much higher than 10^{-4} mhos/meter.

If a permeable ($\mu > \mu_o$) shell exists in the moon, the arrival of a step transient at the moon would cause induction of a steady dipolar field which would have a magnetic moment aligned along the external field direction [see *Jackson,* 1962]. This induced dipolar field, as measured on the lunar surface, would have a radial component in the same direction as the radial component of the external field, whereas the tangential components of the induced and external fields would be of opposite polarity. These properties would cause the radial ratio $\Delta B_{Ax}/\Delta B_{Ex}$ to be greater than 1 and the tangential ratios $\Delta B_{Ay,z}/\Delta B_{Ey,z}$ to be less than 1, in direct contrast to the measured characteristics of Figure 12.

In order to examine the toroidal field induction mode, it is necessary to consider the geometric properties of a toroidal field. For a spherically symmetric moon, the toroidal mode has no radial component at the lunar surface (refer to Figure 2b and *Sill and Blank,* 1970) and therefore would not describe the radial data shown in Figure 12a. Furthermore, the toroidal field has cylindrical rather than dipolar geometry (see Figure 2b), and its orientation depends on both the solar-wind velocity direction and the external field $\vec{B}_E$ direction. Thus the orientation of the toroidal field at a given surface site would be independent of the poloidal field direction and, in general, could either aid or oppose the poloidal field tangential component. For many transient events, therefore, the toroidal mode would cause the points in the Figure 12 tangential curves to be scattered about the reference line of slope equal to 1 rather than to lie

along a line of slope greater than 1. Consequently, a toroidal response mode would not explain the deviation of the data from the two-layer model.

The third alternative, that of a highly conducting core deep in the lunar interior, would cause the trends indicated in all three graphs of Figure 12. For this case, the eddy-current decay time for the deep core would be much longer than that in the outer regions, causing a poloidal field to persist long after the currents in the outer regions have decayed. This deep core eddy-current field, which would persist much longer than four minutes, would cause the Apollo 12 radial component to fall short of the Explorer 35 post-transient value as shown in Figure 12a and would cause the Apollo 12 tangential component, after the initial overshoot, to fall short of the corresponding Explorer 35 value (Figures 12b and 12c). The deep core, therefore, would produce the characteristics of the measured deviations from the two-layer mode as illustrated in Figure 12.

Properties of the three-layer moon. Figure 13 schematically shows the three-layer conductivity model of the moon and depicts a time sequence of field-line configurations for a magnetic step transient. At $t = 0$ the external field changes from an initial value $\vec{B}_{Eo}$ to a final value $\vec{B}_{Ef}$. For the outer crust, $\sigma_o \to 0$, so its eddy-current decay time $\tau_o \to 0$, and for the intermediate shell and inner core, respectively, $\sigma_1 << \sigma_2$ so that $\tau_1 << \tau_2$. The external field instantaneously diffuses into the nonconducting crust, but eddy currents are induced inside the two inner layers, and further penetration of the external field is temporarily prevented. For $0 < t < 4$ minutes ($4 \text{ minutes} \simeq 5\tau_1$), eddy currents decay inside the intermediate layer, allowing the external field to diffuse into that layer. For times in the range $4 \text{ minutes} < t < \tau_2$, eddy currents in the highly conducting

Fig. 13

inner core start to decay and the external field diffuses through the entire sphere after some extended time $t >> \tau_2$.

Transient events which persist long enough to permit study of this long-term decay of inner-core currents (i.e., events which show a sharp step change in Explorer 35 external-field data, followed by a long period of steady field) are rare, but four good cases have been found, and two are presented here. Figure 14 shows the two long-term events, both of which last over 15 minutes with nominal amplitude fluctuations of about 1 gamma before and after the transient arrival at $t = 0$. Limits on the conductivity and radius of the inner core were found by fitting the theoretical function $F(t)$ of equation (8) to the data for times greater than four minutes after transient arrival (at which time currents in the intermediate shell will have decayed and the inductive interaction between the inner core and the intermediate shell can be neglected). The parametric fit yields a lower limit of $\sigma_2 \sim 10^{-2}$ mhos/meter and an upper limit of $R_2 \sim 0.6R_m$.

Fig. 14

It is assumed that the conductivity calculated for the two-layer-model core will approximate the conductivity of the three-layer-model intermediate shell. This is reasonable since the intermediate region in the three-layer model has a volume ≥ 4 times that of the inner core, and thus eddy-current decay characteristics of the intermediate shell should not be significantly changed by the more highly conducting inner core. An upper limit is not calculated for σ_2 since a very small inner core ($R_2 < 0.2R_m$) could have very high conductivity, but its poloidal field, which would be reduced by a factor $(R_2/R_m)^3$ at the lunar surface, would not be detectable above the instrument threshold of 0.2 gamma for a 10-gamma step transient.

It is concluded, therefore, that the most probable cause of the discrepancy between the data and the two-layer model is the lack of homogeneity of the conducting sphere. A model which has a continuously varying conductivity distribution will be used in future work to give a more thorough description of the conductivity of the lunar interior. At the present time, however, the simplest model which qualitatively explains the general aspects of the dark-side transient-response data is a three-layer model having a thin outer crust of very low conductivity (i.e., conductivity so low that field changes diffuse through the crust in times too short to be detected by the Apollo 12 magnetometer), an intermediate layer of conductivity $\sigma_1 \sim 10^{-4}$ mhos/meter, and a deep conducting core of conductivity σ_2 greater than 10^{-2} mhos/meter.

Internal temperature calculations. The electrical conductivity values obtained by measuring the time response characteristics of the vector magnetic field transient can be used to calculate the internal temperature distribution if the material composition is known. For materials and pressures that have been used to model the lunar interior (see, e.g., *Urey*, 1970; *Kopal*, 1969), the electrical conductivity is independent of pressure to a first approximation [*England et al.*, 1968; *Rikitake*, 1966]. The conductivity can be expressed as

$$\sigma = a_1 \exp(-E_1/kT) + a_2 \exp(-E_2/kT) \qquad (9)$$

where E_1 and E_2 are the activation energies of the intrinsic semiconduction mechanism and ionic conduction, respectively; a_1 and a_2 are material-dependent constants, k is Boltzmann's constant, and T is the temperature of the material in degrees Kelvin. The electrical conductivity has been measured as a function of temperature for several materials which may

comprise the bulk of the lunar interior [*Keller and Frischknecht*, 1966; *Nagata*, 1970]. A plot of these measured conductivities versus temperature is shown in Figure 15. Fig. 15

A lunar cross section showing a temperature-conductivity profile of a three-layer lunar interior is given in Figure 16. This figure lists the Fig. 16 electrical conductivities determined by Apollo 12 magnetic-field measurements, and temperatures corresponding to these conductivities for four materials used here to model the lunar-interior composition: olivine, peridotite, basalt, and an Apollo 11 lunar surface sample.

In this paper, the analysis permits consideration of only a lower limit of the inner core temperature. The upper temperature limit for a lunar core has been set at ~1800° K by other investigators [*Fricker et al.*, 1967; *Urey*, 1970] from lunar thermodynamic and internal stress considerations.

SUMMARY AND CONCLUSIONS

The response of the moon to magnetic-field step transients in the solar wind has been investigated for seventy-five events, using simultaneous data from the Apollo 12 lunar surface magnetometer and the lunar orbiting Explorer 35 magnetometer. These transient events were all selected at times when the moon was in the free-streaming solar wind and the Apollo 12 magnetometer was on the lunar dark side.

In order to calculate the internal electrical conductivity, a spherically symmetric two-layer model of the moon was assumed, in which a conducting core is surrounded by a nonconducting crust. Solutions of Maxwell's equations for the induced eddy-current response of this two-layer model show a characteristic damped response in the radial component

and overshoot in the tangential components. The lunar-nighttime Apollo 12 magnetometer data consistently show this distinct difference between radial and tangential components for all step transients; this property strongly implies that the surface magnetometer is indeed measuring a global rather than a local effect.

A best fit of two-layer theory to the data for twenty transients yields the values of conductivity $\sigma_1 = 1.7 \pm 0.4 \times 10^{-4}$ mhos/meter and radius $0.95 \leq R_1 < R_m$ for the conducting core.

The data deviate from the two-layer model in that the post-transient decaying surface field does not approach the proper theoretically predicted asymptote. In order to explain this deviation, possibilities of significant perturbations due to either a lunar permeable shell or a non-negligible toroidal field are considered and qualitatively discounted. The most plausible explanation of the discrepancy is the existence of a deep core with minimum conductivity $\sigma_2 \sim 10^{-2}$ mhos/meter and maximum radius $R_2 \sim 0.6R_m$.

It is concluded, therefore, that the simplest model which qualitatively explains all the general aspects of the dark-side transient-response data is a spherically symmetric three-layer model having a thin outer crust of very low conductivity. The intermediate layer, of radial thickness $R_1 - R_2$ where $0.95R_m \leq R_1 < R_m$ and $R_2 \leq 0.6R_m$, has an electrical conductivity $\sigma_1 = 1.7 \pm 0.4 \times 10^{-4}$ mhos/meter; the inner core has a maximum radius $R_2 \sim 0.6R_m$ and minimum conductivity $\sigma_2 \sim 10^{-2}$ mhos/meter.

The conductivities calculated for the three-layer model are related to the temperatures in the three regions. Temperatures are calculated for four possible lunar material compositions. For the example of an olivine moon, the temperatures of the layers are as follows: crust, $\leq 530°$ K; intermediate layer, $840°$ K; core, $\leq 1240°$ K.

Acknowledgments. The authors wish to thank the Apollo 12 Program Office, Astronauts Charles Conrad, Alan Bean, and Richard Gordon, and the Manned Spacecraft Center Science and Engineering Directorate for the direct participation in carrying out this experiment. We also thank the many individuals at Ames Research Center for the decisive help in program planning, experiment design, and contract monitoring. The instrument was fabricated by Philco-Ford Space and Reentry Systems Division, calibrated at the Goddard Space Flight Center, and integrated with the Apollo Lunar Surface Experiments Package by Bendix Aerospace Corporation. Special thanks go to Dr. Thomas J. Mucha and to Kenneth E. Lewis, Karen Neier, Marion Legg, and their team members for help in data reduction.

APPENDIX

The particular case of the response of the lunar sphere to a step-function transient magnetic field can be treated by extending the theory of *Smythe* [1950]. Here the moon is considered to be a two-layer sphere (see Figure 5) subject to the following conditions:

1. The model is spherically symmetric and has a homogeneous inner core with electrical conductivity σ_1 and radius R_1 surrounded by a non-conducting ($\sigma_o \to 0$) outer shell of thickness ($R_m - R_1$). It is also assumed that the toroidal induction mode is negligible, a condition consistent with a nonconducting outer shell.

2. The sphere is in a vacuum, i.e., no plasma interactions.

3. The sphere is everywhere isotropic and it has constant permeability (μ), permittivity (ε), and conductivity (σ_1). The permeability is everywhere that of free space ($\mu = \mu_o$).

4. Dimensions of external field transients are large compared to the lunar sphere, such that the sphere responds as a whole to the transients.

5. Conduction currents dominate displacement currents within the sphere.

6. There is no net charge on the sphere.

Then, for a coordinate system fixed in the sphere, Maxwell's equations and Ohm's law in the rationalized m.k.s. system are as follows:

$$\vec{\nabla} \times \vec{E} = - \frac{\partial \vec{B}}{\partial t} \tag{A1}$$

$$\vec{\nabla} \times \vec{B} = \mu_o \vec{J} \tag{A2}$$

$$\vec{\nabla} \cdot \vec{B} = 0 \tag{A3}$$

$$\vec{\nabla} \cdot \vec{E} = 0 \tag{A4}$$

$$\vec{J} = \sigma_1 \vec{E} \tag{A5}$$

where $\vec{E}$ and $\vec{B}$ are electric field and magnetic induction, $\vec{J}$ is conduction current density, σ_1 is the electrical conductivity of the sphere's inner core, and $\mu_o = 4\pi \times 10^{-7}$ henrys/meter, the permeability of free space.

By introducing the magnetic vector potential $\vec{A}$, defined by $\vec{\nabla} \times \vec{A} = \vec{B}$ and $\vec{\nabla} \cdot \vec{A} = 0$, one can derive from the above equations the expressions:

$$\nabla^2 \vec{A}_o = 0 \tag{A6}$$

$$\nabla^2 \vec{A}_1 = \mu_o \sigma_1 \frac{\partial \vec{A}_1}{\partial t} \tag{A7}$$

where A_o and A_1 are magnetic vector potentials outside and inside the conducting core, respectively.

If a spherical coordinate system $(\hat{r}, \hat{\theta}, \hat{\phi})$, shown in Figure 5, is chosen such that the magnetic field is independent of $\hat{\phi}$ and has no component in the $\hat{\phi}$ direction, then $\vec{A}$ must lie entirely along $\hat{\phi}$:

$$\vec{A} = A_\phi(r, \theta, t)\hat{\phi} \tag{A8}$$

Then, in equation (A7),

$$\mu_o \sigma_1 \frac{\partial \vec{A}_1}{\partial t} = \mu_o \sigma_1 \frac{\partial A_{1\phi}}{\partial t} \hat{\phi} \tag{A9}$$

and

$$\nabla^2 \vec{A}_1 = \left[\nabla^2 A_{1\phi} - \frac{A_{1\phi}}{r^2 \sin^2 \theta} \right] \hat{\phi} \tag{A10}$$

and equation (A7) becomes

$$\mu_o \sigma_1 \frac{\partial A_{1\phi}}{\partial t} = \nabla^2 A_{1\phi} - \frac{A_{1\phi}}{r^2 \sin^2 \theta} \tag{A11}$$

Expanding the Laplacian, equation (A9) becomes

$$\mu_o \sigma_1 \frac{\partial A_{1\phi}}{\partial t} = \frac{1}{r^2} \frac{\partial}{\partial r} \left(r^2 \frac{\partial A_{1\phi}}{\partial r} \right) + \frac{(1 - u^2)^{1/2}}{r^2} \frac{\partial^2}{\partial u^2} [(1 - u^2)^{1/2} A_{1\phi}] \tag{A12}$$

where $u = \cos \theta$.

Equations (A6) and (A7) can therefore be expressed as:

$$\nabla^2 A_o = 0 \tag{A13}$$

$$\nabla^2 A_1 = \mu_o \sigma_1 \frac{\partial A_1}{\partial t} \tag{A14}$$

Product solutions of these equations are found from equations of the form of (A12):

$$\vec{A}_o = \hat{\phi} \sum_s D_s r^{-2} \sin\theta \exp(-k_s^2 R_1^2 t/\beta^2) \tag{A15}$$

$$\vec{A}_1 = \hat{\phi} \sum_s C_s r^{-1/2} J_{3/2}(k_s r) \sin\theta \exp(-k_s^2 R_1^2 t/\beta^2) \tag{A16}$$

where $J_{3/2}$ is a fractional-order Bessel function and R_1 is the radius of the conducting sphere. The terms C_s, D_s, k_s^2, and β^2 will be determined by applying the appropriate boundary conditions.

Consider, at $t = 0$, a step change $\Delta\vec{B}_{Eo}$ in the external driving magnetic field, from an initial external field $\vec{B}_{Eo}$ to a final field $\vec{B}_{Ef}$; i.e., $\vec{B}_{Ef} = \vec{B}_{Eo} + \Delta\vec{B}_E$. The coordinate system is chosen such that all three of these vectors lie in the plane containing $\hat{r}$ and $\hat{\theta}$ (see Figure 5). Then, by applying boundary conditions across the surface of the conducting core,

$$\vec{A}_o = \vec{A}_1 \tag{A17}$$

$$\mu_o \frac{\partial}{\partial r}(r\vec{A}_o) = \mu_o \frac{\partial}{\partial r}(r\vec{A}_1) , \tag{A18}$$

one can evaluate D_s and β^2 for equation (A16):

$$D_s = \frac{3\,|\Delta\vec{B}_E|\,R_1}{k_s^2} \tag{A19}$$

$$\beta^2 = \mu_o \sigma_1 R_1^2 , \tag{A20}$$

and k_s is a nontrivial eigenvalue of the characteristic equation

$$R \frac{d}{dR}[J_{3/2}(k_s R_1)] + \frac{3}{2} J_{3/2}(k_s R_1) = 0 . \tag{A21}$$

Equation (A21) can be solved to yield the eigenvalues

$$k_s R_1 = s\pi \qquad s = 1, 2, 3, \ldots \tag{A22}$$

The transient potential outside the conducting core is then

$$\vec{A}_o = \hat{\phi}\left[\frac{3\,|\vec{\Delta B}_E|\,R_1^3}{\pi^2 r^2} \sum_{s=1}^{\infty} \frac{1}{s^2} \exp\left(-\frac{s^2\pi^2 t}{\beta^2}\right)\right] \sin\theta \tag{A23}$$

Since the transient poloidal magnetic field induced in the sphere is derivable as the curl of the vector potential, the components of the poloidal transient field $\vec{B}_p$ on the outer surface of the sphere at $r = R_m$ are

$$B_{pr} = \frac{1}{r \sin\theta} \frac{\partial}{\partial t} (A_o \sin\theta) = -2Q\,|\vec{\Delta B}_E|\,F(t) \cos\theta \tag{A24}$$

$$B_{p\theta} = -\frac{1}{r} \frac{\partial}{\partial r} (rA_o) = -Q\,|\vec{\Delta B}_E|\,F(t) \sin\theta \tag{A25}$$

$$B_{p\phi} = 0 \tag{A26}$$

where

$$Q = \frac{3}{2}\,(R_1/R_m)^3 \tag{A27}$$

$$F(t) = \frac{2}{\pi^2} \sum_{s=1}^{\infty} \frac{1}{s^2} \exp(-s^2\pi^2 t/\beta^2) \tag{A28}$$

$$\beta^2 = \mu_o \sigma_1 R_1^2 \tag{A29}$$

A plot of $F(t)$ appears in Figure 6.

In order to compare actual measurements to this two-layer theory, it is advantageous to transform equations (A24), (A25), and (A26) from the spherical system $(\hat{r}, \hat{\theta}, \hat{\phi})$ to the $(\hat{x}, \hat{y}, \hat{z})$ system, which has its origin at the Apollo 12 magnetometer site where $r = R_m$. Here $\hat{x}$ is directed radially outward from the lunar surface and $\hat{y}$ and $\hat{z}$ lie tangential to the surface, directed eastward and northward, respectively. This transformation is accomplished by the transformation matrix

$$\begin{pmatrix} 1 & 0 & 0 \\ 0 & \cos\Psi & \sin\Psi \\ 0 & -\sin\Psi & \cos\Psi \end{pmatrix} \tag{A30}$$

which rotates the $(\hat{r}, \hat{\theta}, \hat{\phi})$ coordinate system into the $(\hat{x}, \hat{y}, \hat{z})$ system (see Figure 5), yielding

$$\left.\begin{aligned} B_{px} &= -2Q\ |\overrightarrow{\Delta B_E}|\ F(t)\cos\theta \\ B_{py} &= -Q\ |\overrightarrow{\Delta B_E}|\ F(t)\sin\theta\cos\Psi \\ B_{pz} &= +Q\ |\overrightarrow{\Delta B_E}|\ F(t)\sin\theta\sin\Psi \end{aligned}\right\} \tag{A31}$$

But in the ALSEP system, $\overrightarrow{\Delta B_E}$ has components $\Delta B_{Ex} = |\overrightarrow{\Delta B_E}|\cos\theta$, $\Delta B_{Ey} = -|\overrightarrow{\Delta B_E}|\sin\theta\cos\Psi$, and $\Delta B_{Ez} = |\overrightarrow{\Delta B_E}|\sin\theta\sin\Psi$, so

$$\left.\begin{aligned} B_{px} &= -2Q(\Delta B_{Ex})F(t) \\ B_{py} &= Q(\Delta B_{Ey})F(t) \\ B_{pz} &= Q(\Delta B_{Ez})F(t) \end{aligned}\right\} \tag{A32}$$

Components of the total field $(\overrightarrow{B_A})$ on the outer surface of the sphere at $r = R_m$ are found by adding components of the external driving field $(\vec{B}_E)$ to components of the induced lunar poloidal field $(\vec{B}_p)$:

$t < 0$:

$$B_{Ax} = B_{Exo} \tag{A33}$$

$$B_{Ay} = B_{Eyo} \tag{A34}$$

$$B_{Az} = B_{Ezo} \tag{A35}$$

$t \geq 0$:

$$B_{Ax} = -2Q(\Delta B_{Ex})F(t) + B_{Exf} \tag{A36}$$

$$B_{Ay} = Q(\Delta B_{Ey})F(t) + B_{Eyf} \tag{A37}$$

$$B_{Az} = Q(\Delta B_{Ez})F(t) + B_{Ezf} \tag{A38}$$

Here B_{Eio} and B_{Eif} (i = x, y, or z) are initial and final external field components, respectively. These solutions are plotted in Figure 7.

REFERENCES

Behannon, K. W., Intrinsic magnetic properties of the lunar body, *J. Geophys. Res.*, *73*, 7257, 1968.

Brown, W. E., Jr., R. A. Dibos, G. B. Gibson, D. O. Muhleman, W. H. Peake, and V. J. Poehls, Lunar surface electrical properties, Surveyor III mission report, part II: Scientific results, *Tech. Rept. 32-1177, Jet Propulsion Laboratory*, 1967.

Chung, D. H., W. B. Westphal, and G. Simmons, Dielectric properties of Apollo 11 lunar samples and their comparison with earth materials, *J. Geophys. Res.*, *75*, 1970.

Colburn, D. S., R. G. Currie, J. D. Mihalov, and C. P. Sonett, Diamagnetic solar-wind cavity discovered behind moon, *Science*, *158*, 1040, 1967.

Dolginov, Sh. Sh., E. G. Eroshenko, L. N. Zhuzgov, and N. V. Pushkov, Investigation of the magnetic field of the moon, *Geomagnetism and Aeronomy*, *1*, 18, 1961.

Dolginov, Sh. Sh., E. G. Eroshenko, L. N. Zhuzgov, and N. V. Pushkov, Measurements of the magnetic field in the vicinity of the moon by the artificial satellite Luna 10, *Akad. Nauk USSR, Doklady*, *170*, 574, 1966.

deWys, J. N., Results and implications of magnetic experiments on Surveyor 5, 6, and 7 spacecrafts (abs.), *Trans. Am. Geophys. Union*, *49*, 249, 1968.

Doell, R. R., G. S. Grommé, A. N. Thorpe, and F. E. Senftle, Magnetic studies of Apollo 11 lunar samples, in *Proceedings of the Apollo 11 Lunar Science Conference, vol. 3*, edited by A. A. Levinson, Pergamon Press, New York, p. 2097, 1970.

Dyal, P., C. W. Parkin, and C. P. Sonett, Apollo 12 magnetometer: measurement of a steady magnetic field on the surface of the moon, *Science*, *169*, 762, 1970*a*.

Dyal, P., C. W. Parkin, and C. P. Sonett, Lunar surface magnetometer, *IEEE Trans. on Geoscience Electronics, GE-8(4)*, 1970b.

England, A. W., G. Simmons, and D. Strangway, Electrical conductivity of the moon, *J. Geophys. Res., 73*, 3219, 1968.

Fricker, P. E., R. T. Reynolds, and A. L. Summers, On the thermal history of the moon, *J. Geophys. Res., 72*, 2649, 1967.

Geyger, W. A., *Nonlinear-Magnetic Control Devices*, McGraw-Hill Book Co., New York, 1964.

Gold, T., The magnetosphere of the moon, in *The Solar Wind*, edited by R. J. Mackin, Jr., and M. Neugebauer, Pergamon Press, New York, 1966.

Gordon, D. I., R. H. Lundsten, and R. A. Chiarodo, Factors affecting the sensitivity of gamma-level ring-core magnetometers, *IEEE Trans. on Magnetics, MAG-1(4)*, 330, 1965.

Hagfors, T., Review of radar observations of the moon, in *The Nature of the Lunar Surface*, edited by W. N. Hess, D. H. Menzel, and J. A. O'Keefe, Johns Hopkins Press, Baltimore, 1966.

Hollweg, J. W., Lunar conducting islands and formation of a lunar limb shock wave, *J. Geophys. Res., 75*, 1209, 1970.

Holt, H. E., and J. J. Rennilson, Photometric and polarimetric properties of the lunar regolith, in *Apollo 12 Preliminary Science Rept., NASA SP-235*, 1970.

Jackson, J. D., *Classical Electrodynamics*, John Wiley and Sons, New York, 1962.

Keller, G. V., and F. C. Frischknecht, *Electrical Methods in Geophysical Prospecting*, Pergamon Press, New York, 1966.

Kopal, Z., *The Moon*, D. Reidel, Dordrecht, Holland, 1969.

Larochelle, A., and E. J. Schwarz, Magnetic properties of lunar sample 10048-22, in *Proceedings of the Apollo 11 Lunar Science Conference, vol. 3*, edited by A. A. Levinson, Pergamon Press, New York, p. 2305, 1970.

Lyon, E. F., H. S. Bridge, and J. H. Binsack, Explorer 35 plasma measurements in the vicinity of the moon, *J. Geophys. Res.*, *72*, 6113, 1967.

Michel, F. C., Magnetic field structure behind the moon, *J. Geophys. Res.*, *73*, 1533, 1968.

Nagata, T., Electrical conductivity and age of the moon, paper M.14, presented at the Thirteenth Plenary Meeting, COSPAR, Leningrad, USSR, 1970.

Nagata, T., Y. Ishikawa, H. Kinoshita, M. Kono, Y. Syono, and R. M. Fisher, Magnetic properties and natural remanent magnetization of lunar materials, in *Proceedings of the Apollo 11 Lunar Science Conference, vol. 3*, edited by A. A. Levinson, Pergamon Press, New York, p. 2325, 1970.

Ness, N. F., Electrical conductivity of the moon (abs.), *Trans. Am. Geophys. Union*, *49*, 242, 1968.

Ness, N. F., Lunar Explorer 35, *Space Res.*, *9*, 678, 1969.

Ness, N. F., K. W. Behannon, C. S. Scearce, and S. C. Cantarano, Early results from the magnetic field experiment on Explorer 35, *J. Geophys. Res.*, *72*, 5769, 1967.

Ness, N. F., K. W. Behannon, H. E. Taylor, and Y. C. Whang, Perturbations of the interplanetary magnetic field by the lunar wake, *J. Geophys. Res.*, *73*, 3421, 1968.

Rikitake, T., *Electromagnetism and the Earth's Interior*, Elsevier, Amsterdam 1966.

Runcorn, S. K., D. W. Collinson, W. O'Reilly, M. H. Battey, A. A. Stephenson, J. M. Jones, A. J. Manson, and P. W. Readman, Magnetic properties of Apollo 11 lunar samples, in *Proceedings of the Apollo 11 Lunar Science Conference, vol. 3*, edited by A. A. Levinson, Pergamon Press, New York, p. 2369, 1970.

Schubert, G., and K. Schwartz, A theory for the interpretation of lunar surface magnetometer data, *The Moon, 1*, 106, 1969.

Serbu, G. P., Explorer 35 measurements of low-energy plasma in lunar orbit, *J. Geophys. Res., 74*, 372, 1969.

Sill, W. R., and J. L. Blank, Method for estimating the electrical conductivity of the lunar interior, *J. Geophys. Res., 75*, 201, 1970.

Smythe, W. R., *Static and Dynamic Electricity*, McGraw-Hill Book Co., New York, 1950.

Snyder, C. W., D. R. Clay, and M. Neugebauer, The solar-wind spectrometer experiment, in *Apollo 12 Preliminary Science Rept., NASA SP-235*, 1970.

Sonett, C. P., D. S. Colburn, and R. G. Currie, The intrinsic magnetic field of the moon, *J. Geophys. Res., 72*, 5503, 1967*a*.

Sonett, C. P., D. S. Colburn, R. G. Currie, and J. D. Mihalov, The geomagnetic tail: topology, reconnection and interaction with the moon, in *Physics of the Magnetosphere*, edited by R. L. Carovillano, J. F. McClay, and H. R. Radoski, D. Reidel Publishing Co., Dordrecht, Holland, 1967*b*.

Sonett, C. P., and D. S. Colburn, Establishment of a lunar unipolar generator and associated shock and wake by the solar wind, *Nature, 216*, 340, 1967.

Spreiter, J. R., M. D. Marsh, and A. L. Summers, Hydromagnetic aspects of solar wind flow past the moon, *Cosmic Electrodynamics, 1*, 5, 1970.

Strangway, D. W., E. E. Larson, and G. W. Pearce, Magnetic studies of lunar samples - breccia and fines, in *Proceedings of the Apollo 11 Lunar Science Conference, vol. 3*, edited by A. A. Levinson, Pergamon Press, New York, p. 2435, 1970.

Tozer, D. C., and J. Wilson, III, The electrical conductivity of the moon, the electrical conductivity of the moon's interior, *Proc. Roy. Soc. (London), A296*, 320, 1967.

Urey, H. C., Origin and history of the moon, in *Physics and Astronomy of the Moon*, edited by Z. Kopal, Academic Press, New York, 1970.

Wait, J. R., A conducting sphere in a time varying magnetic field, *Geophysics, 16*, 666, 1951.

Ward, S. H., Gross estimates of the conductivity, dielectric constant and magnetic permeability distributions in the moon, *Radio Sci., 4*, 117, 1969.

Whang, Y. C., Interaction of the magnetized solar wind with the moon, *Phys. Fluids, 11*, 969, 1968.

TABLE 1. Apollo 12 Magnetometer Characteristics

Parameter	Value
Range	0 to ±400 gammas 0 to ±200 gammas 0 to ±100 gammas
Resolution	±0.2 gamma
Frequency response	dc to 3 Hz
Angular response	Proportional to cosine of angle between magnetic-field vector and sensor axis
Sensor geometry	Three orthogonal sensors at the end of 100-cm booms Orientation determination to within 1° in lunar coordinates
Commands	10 ground and 1 spacecraft
Analog zero determination	180° flip of sensor
Internal calibration	0, ±25, ±50, and ±75% of full scale
Field bias offset capability	0, ±25, ±50, and ±75% of full scale
Modes of operation	Orthogonal field measurements Gradient measurement Internal calibration
Power	3.5 W average in daytime 7.5 W average in nighttime
Weight	8.9 kg
Size	25 × 28 × 63 cm
Operating temperature	-50° to +85°C

FIGURE CAPTIONS

Figure 1. Lunar orbit projection onto the solar ecliptic plane, showing the Apollo 12 magnetometer during the first post-deployment lunation, 1969. During a complete revolution around the earth, the magnetometer passes through the earth's bow shock, the magnetosheath, the geomagnetic tail, and the interplanetary region dominated by solar plasma fields.

Figure 2. Induced lunar magnetic fields. (a) Poloidal field $\vec{B}_p$, induced by time-dependent fluctuations in the solar magnetic field. The lunar equatorial plane, the solar magnetic field $\vec{B}_E$, and the velocity $\vec{v}$ of the moon with respect to the solar wind are in the plane of the paper. (b) Toroidal field $\vec{B}_t$, induced by a $\vec{v} \times \vec{B}_E$ driving electric field. The electrical field exists due to the motion of the external solar magnetic field $\vec{B}_E$, frozen in the solar wind, past the moon. View shows the side of the moon facing the sun with lunar north pole at top.

Figure 3. The Apollo 12 lunar surface magnetometer deployed on the moon in Oceanus Procellarum. Sensors are at the top ends of the booms and approximately 75 cm above the lunar surface. The sensor boom shown at right is directed east. The electronics and the motor drive assembly are located in the box, encased in a thermal blanket. Heat rejection during lunar day and retention during lunar night are controlled by a parabolic reflector array on two sides of the electronics box. The astronaut bubble level and azimuthal shadowgraph, which allow accurate orientation of the magnetometer, are on top of the box. Power, digital signals, and commands are conveyed through a ribbon

cable, which connects to the ALSEP central station telemetry receiver and transmitter. Astronaut Conrad is shown in the background, adjusting the S-band antenna on the central station.

Figure 4. Explorer 35 orbit around the moon, projected onto the solar ecliptic plane. The period of revolution is 11.5 hours. This particular orbit shows the nighttime positions of the Apollo 12 and Explorer 35 magnetometers at the time of the transient event shown in Figure 11.

Figure 5. Coordinate systems. The orthogonal set $(\hat{r}, \hat{\theta}, \hat{\phi})$ forms a spherical system; the external driving field step change $\overrightarrow{\Delta B}_E$ and the radius vector to the Apollo 12 site lie in the $\hat{r} - \hat{\theta}$ plane. The orthogonal set $(\hat{x}, \hat{y}, \hat{z})$ forms a coordinate system where the origin is at the surface magnetometer position and $\hat{x}$, $\hat{y}$, $\hat{z}$ are directed radially outward from the surface, tangentially eastward, and tangentially northward, respectively.

Figure 6. Time-dependent portion $F(t)$ of the two-layer model surface-field response solution for a step-function transient in the driving solar magnetic field (see equation (8)). σ_1 and R_1 are conductivity and radius, respectively, of the core.

Figure 7. Theoretical solutions (plots of equations (8) through (10)) for the poloidal magnetic-field response of a homogeneous conducting lunar core of radius R_1 to a step-function transient in the driving solar-wind magnetic field. For a step-function change $\overrightarrow{\Delta B}_E$ in the external driving field (measured by Explorer 35), the total magnetic field at the surface of the moon $\vec{B}_A$ (measured by the Apollo 12 magnetometer) will be damped in the radial (B_{Ax}) component and will

overshoot in the tangential (B_{Ay} and B_{Az}) components. A family of curves is shown for different values of the parameter R_1/R_m.

Figure 8. Response to step-function transients in all three vector components. The components are expressed in a coordinate system which has its origin on the lunar surface at the Apollo 12 site. The x-axis is directed radially outward from the lunar surface; y and z are tangential to the surface, directed eastward and northward, respectively. Note damping on the radial x-axis and overshoot on tangential y and z axes. Apollo 12 and Explorer 35 data scales differ due to the existence of a 36 ± 5 gamma steady field at the Apollo 12 site.

Figure 9. X-axis (radial) response to a double square wave. Note distinct damping in Apollo 12 x-axis data for each of the four step transients in simultaneous Explorer 35 data.

Figure 10. Y-axis (tangential) response to a step transient, showing distinct overshoot in Apollo 12 y-axis data.

Figure 11. Comparison between Apollo 12 magnetometer data and two-layer lunar model theory for an x-axis (radial) step transient. Best fit is for a homogeneous core of conductivity $\sigma = 1.5 \times 10^{-4}$ mhos/meter and radius $0.95R_m \leq R < R_m$. Superimposed theoretical decay curves for other core conductivities illustrate the sensitive dependence of decay characteristics on the conductivity. This transient event occurred at a time when the Apollo 12 magnetometer was on the lunar dark side and Explorer 35 was in the free-streaming solar wind (see Figure 4).

Figure 12. Differences between field component values measured at $t = 0$ and at $t = +4$ minutes in the Apollo 12 data (ΔB_{Ai}), plotted versus

corresponding differences in the Explorer 35 data (ΔB_{Ei}). Each point represents a separate transient event occurring when the Apollo 12 magnetometer was on the lunar dark side. A reference line of slope one is shown on each plot, indicating the functional dependence of ΔB_{Ai} on ΔB_{Ei} for a two-layer model which decays to an asymptotic value within four minutes. Deviations of the data from the reference line indicate that currents are still flowing in a deep lunar core at times $t > 4$ minutes. (a) Radial x-axis. (b) Tangential y-axis. (c) Tangential z-axis.

Figure 13. A graphical representation of the total-field poloidal response of a three-layer sphere to a step directional change in the external driving field. The external field changes at $t = 0$ from an initial value $\vec{B}_{Eo}$ to a final $\vec{B}_{Ef}$ by the vector quantity $\Delta\vec{B}_E = \vec{B}_{Ef} - \vec{B}_{Eo}$. For the outer crust $\sigma_o \sim 0$ so its decay time constant $\tau_o \sim 0$, and for the inner layers $\sigma_1 << \sigma_2$ so $\tau_1 << \tau_2$. (a) Initial condition at $t < 0$. (b) External field has changed direction; the field has instantaneously penetrated the outer nonconducting shell and is diffusing into the middle shell. (c) Poloidal currents have mostly decayed in the middle shell, but they are still freely flowing in the highly conducting core. (d) Final state after a time long enough for eddy currents to have decayed throughout the sphere, allowing the external field to penetrate the entire sphere.

Figure 14. Extended time response of the moon to step transients. (a) Z-axis (tangential) event showing gradual decay of the surface field over a 15-minute time span. (b) X-axis (radial) event.

Figure 15. Electrical conductivity as a function of temperature for some possible lunar interior materials.

Figure 16. Temperature and conductivity contours for a three-layer moon.

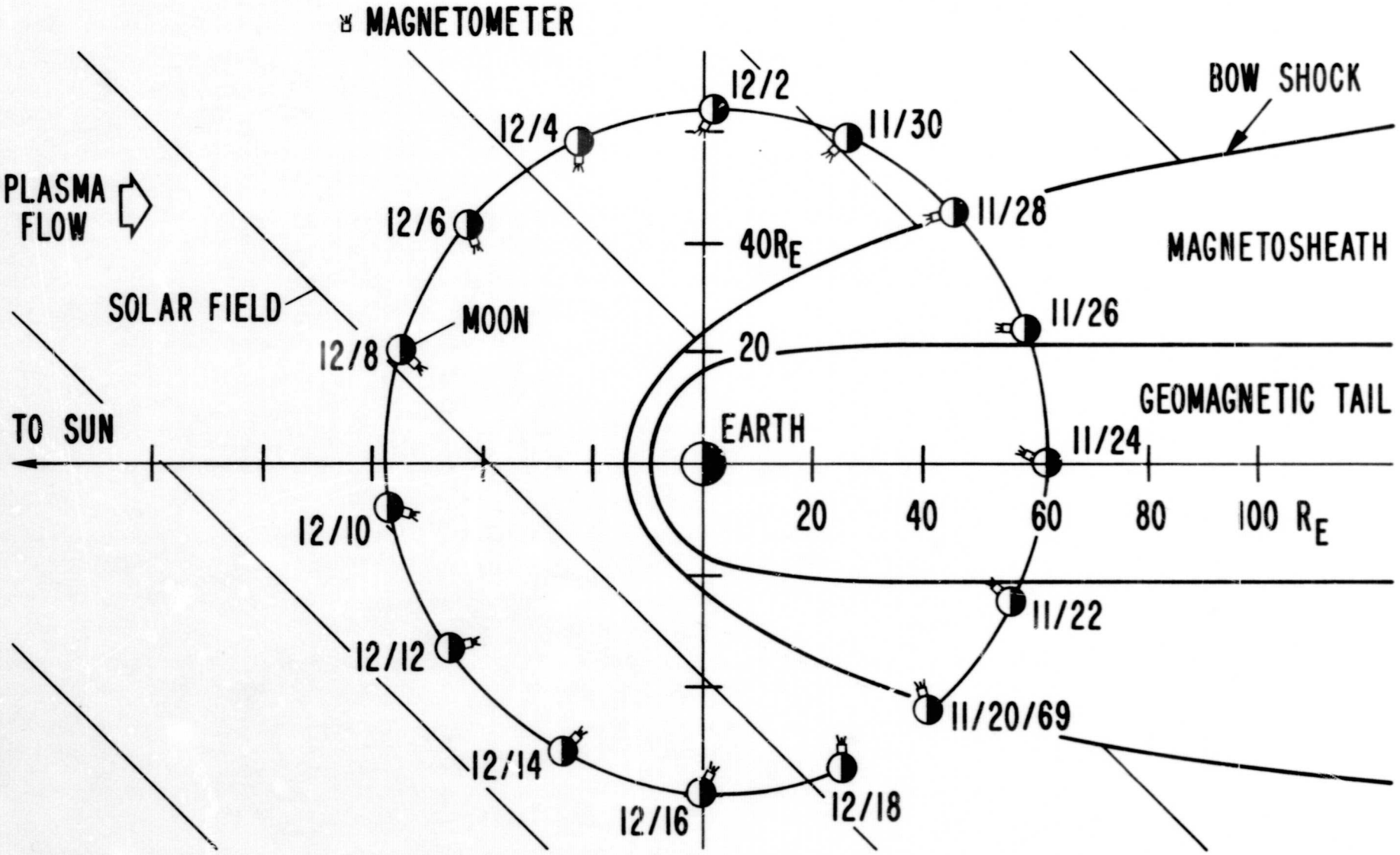
MAGNETOMETER
PLASMA FLOW
SOLAR FIELD
MOON
TO SUN
EARTH
BOW SHOCK
MAGNETOSHEATH
GEOMAGNETIC TAIL
40R_E
20
12/2
12/4
12/6
12/8
12/10
12/12
12/14
12/16
12/18
11/30
11/28
11/26
11/24
11/22
11/20/69
20
40
60
80
100 R_E

Figure 1.

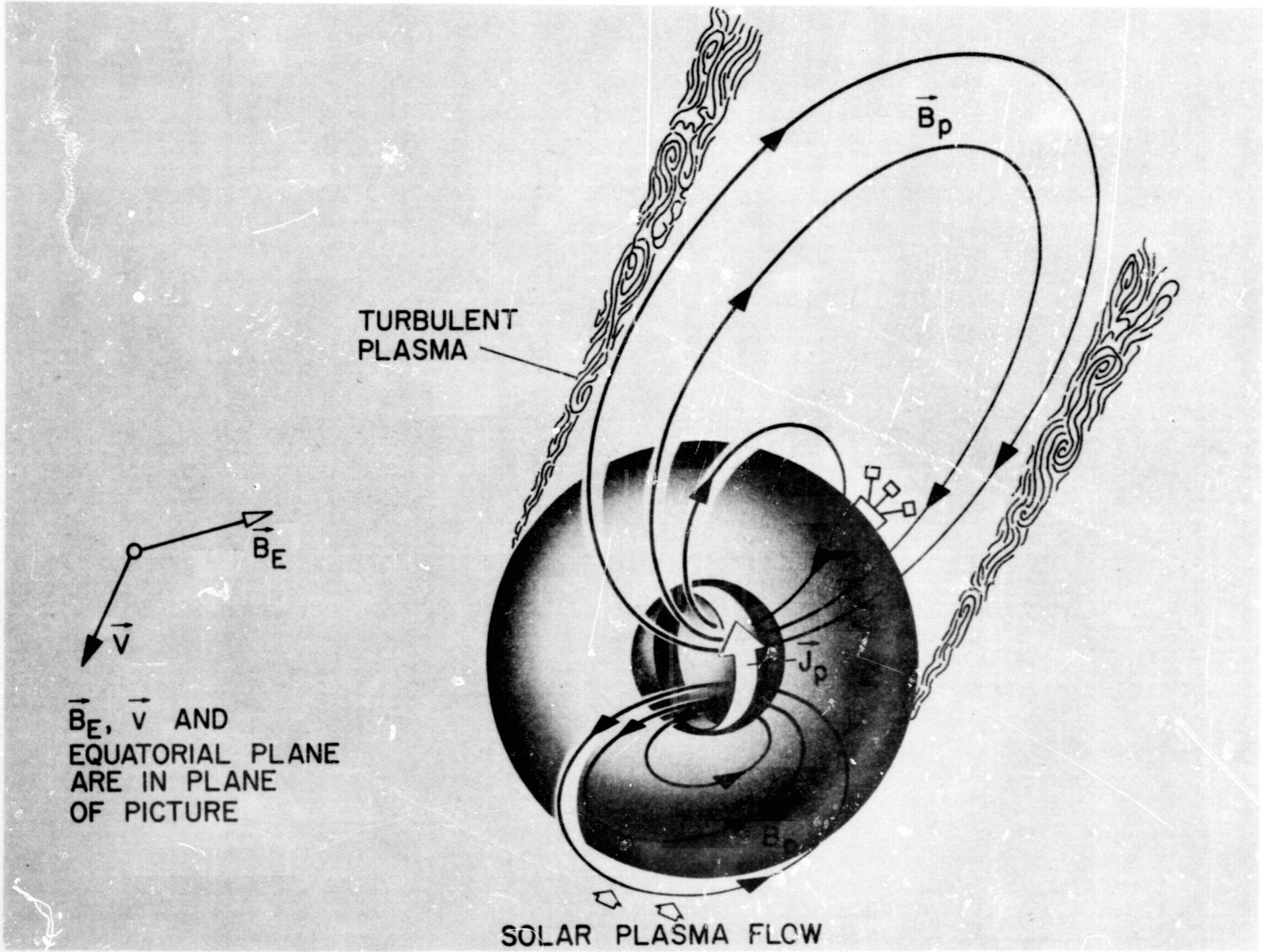
TURBULENT
PLASMA
$\vec{B}_p$
$\vec{B}_E$
$\vec{V}$
$\vec{B}_E$, $\vec{V}$ AND
EQUATORIAL PLANE
ARE IN PLANE
OF PICTURE
$\vec{J}_p$
B_p
SOLAR PLASMA FLOW

Figure 2(a).

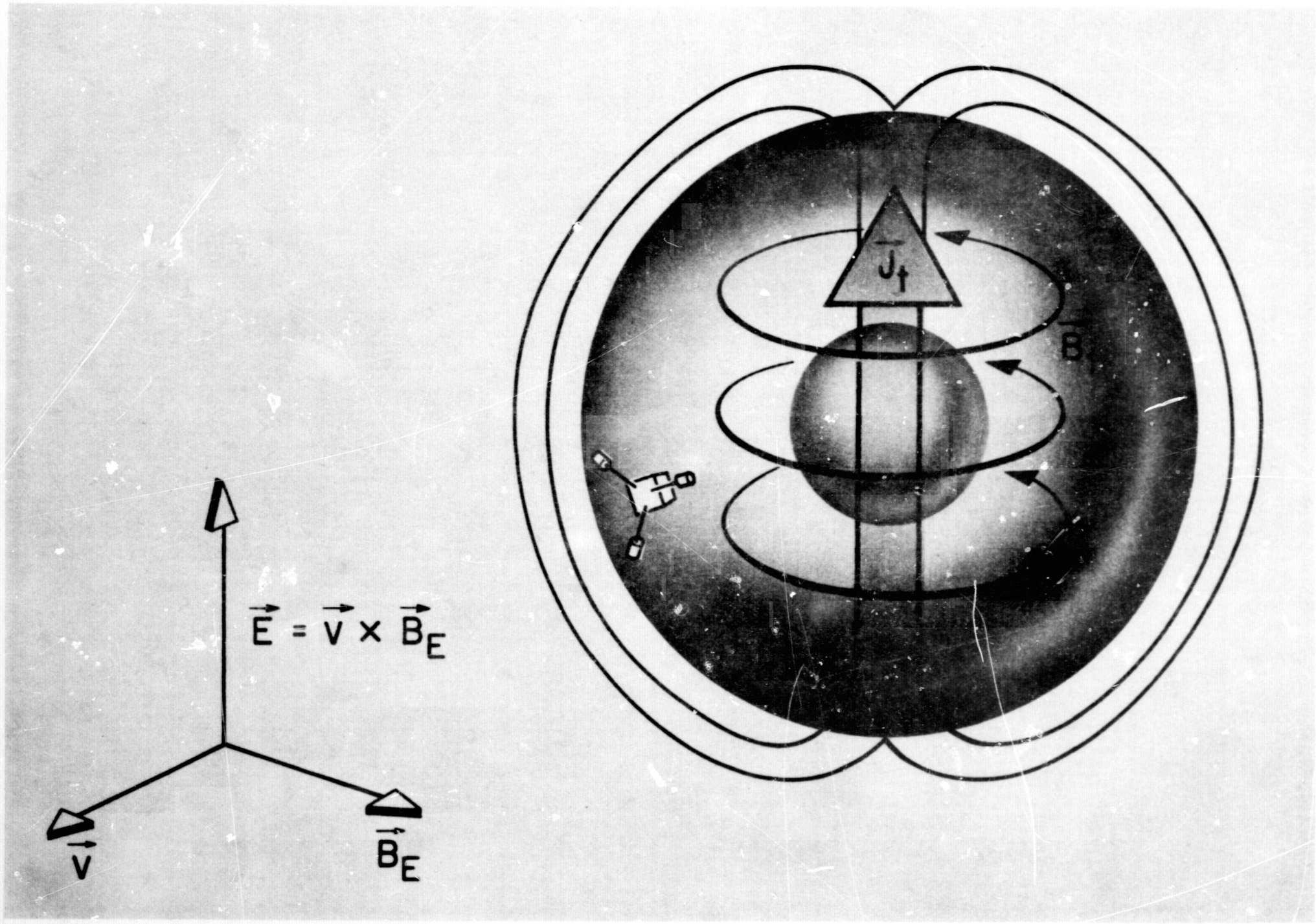

Figure 2(b).

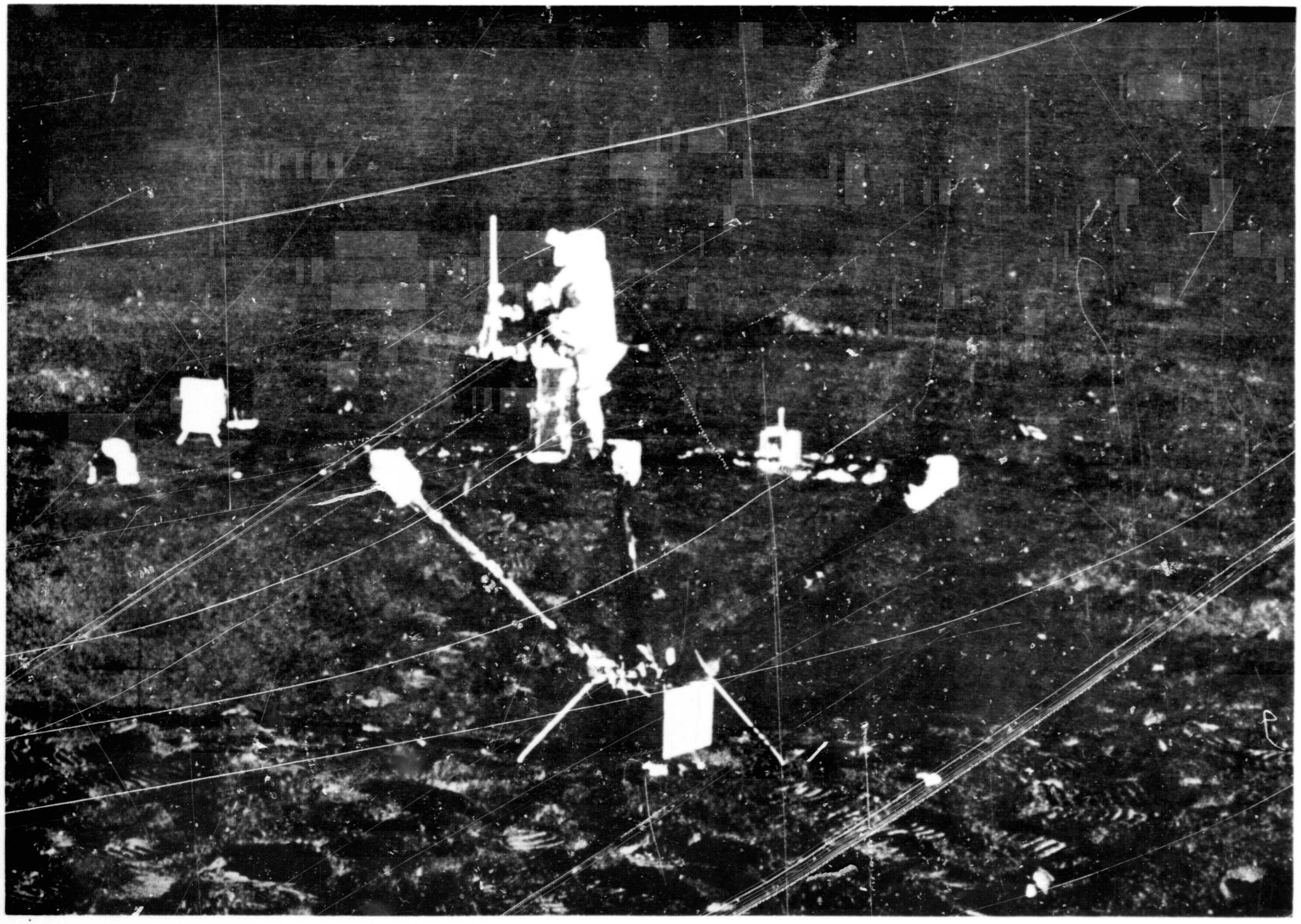

Figure 3.

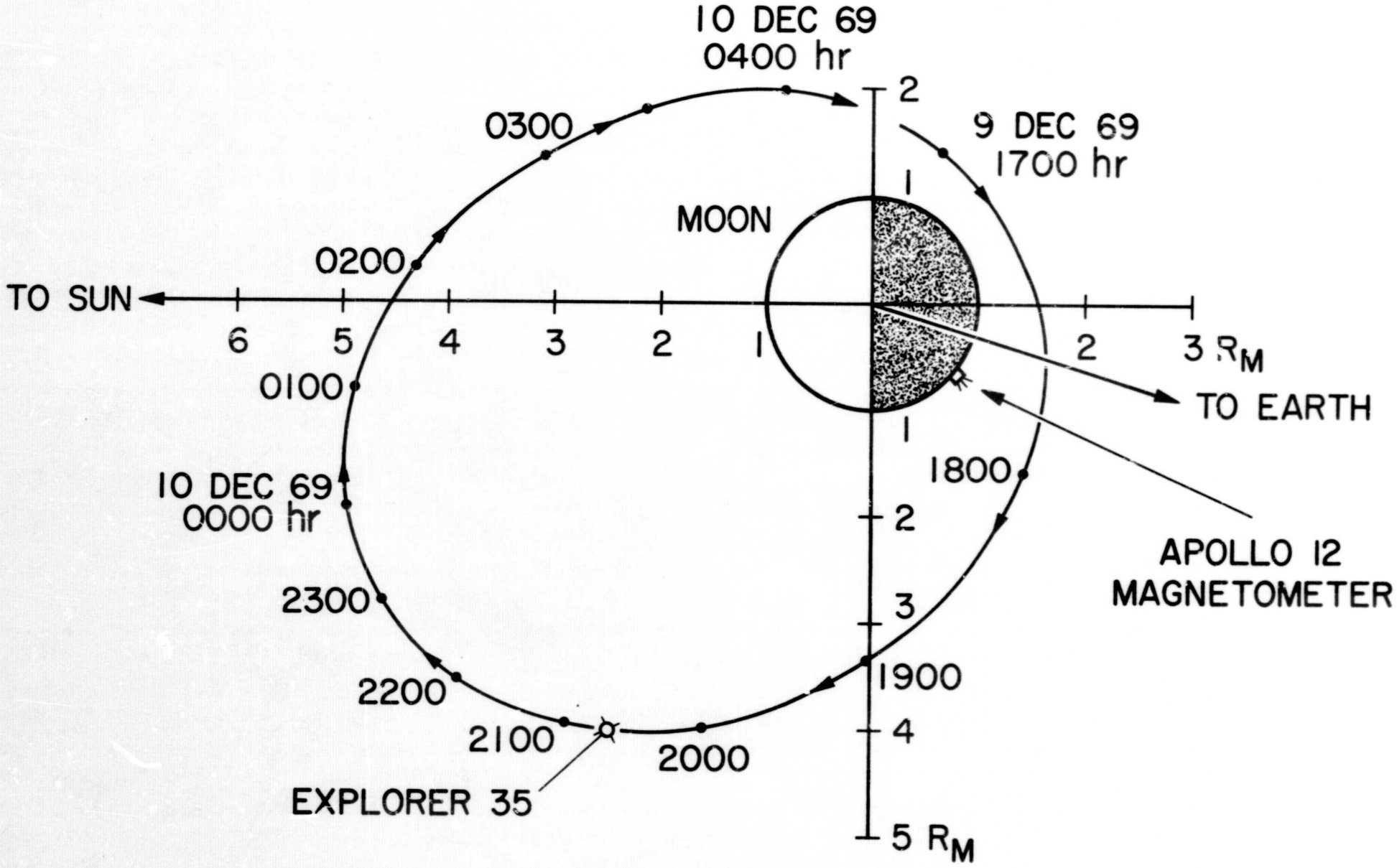
10 DEC 69
0400 hr
0300
0200
0100
10 DEC 69
0000 hr
2300
2200
2100
2000
EXPLORER 35
TO SUN
6
5
4
3
2
1
MOON
2
1
2
3 R_M
TO EARTH
1
1800
2
3
1900
4
5 R_M
9 DEC 69
1700 hr
APOLLO 12
MAGNETOMETER

Figure 4.

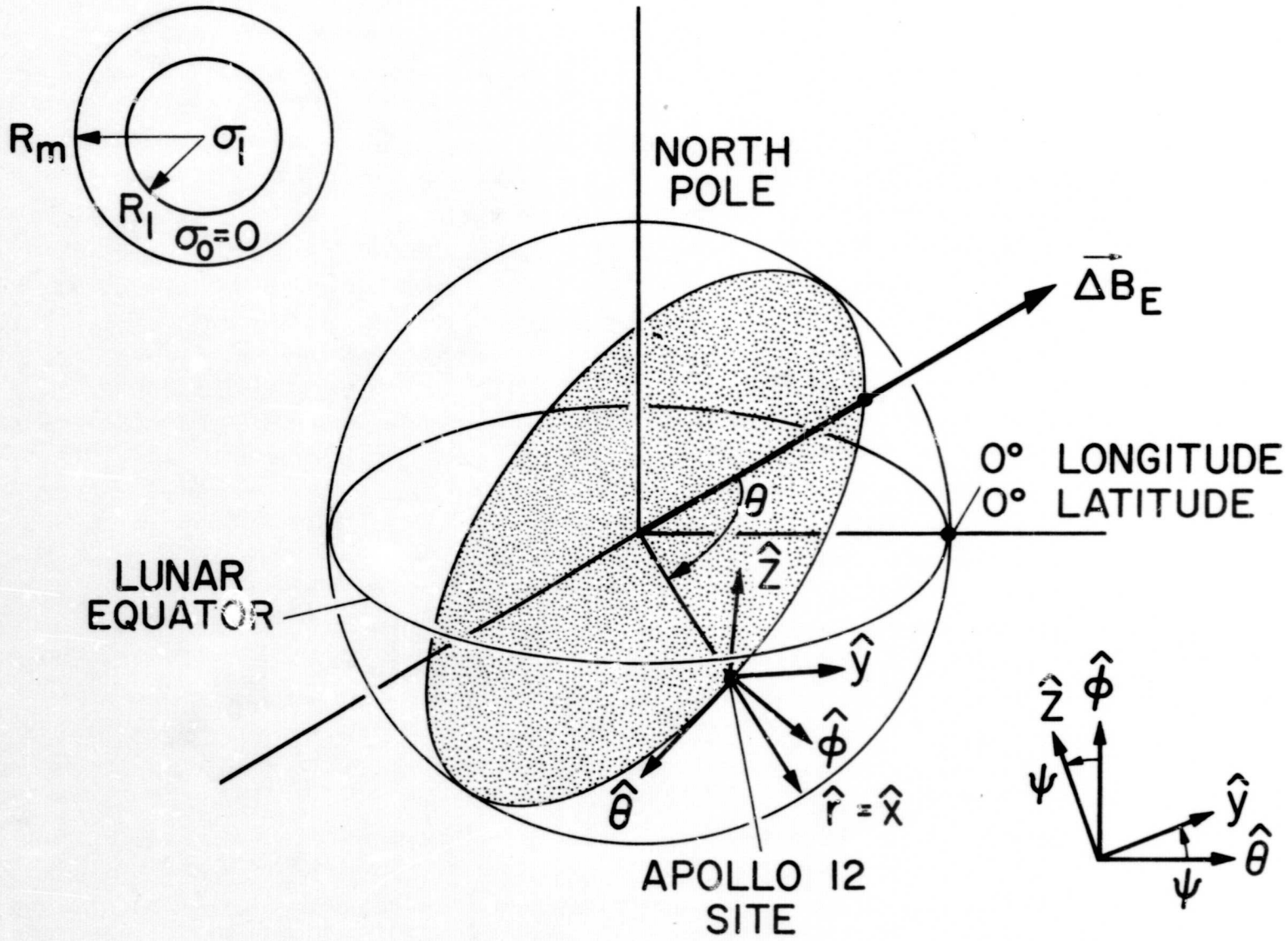
R_m
σ_1
R_1
$\sigma_0=0$
NORTH
POLE
$\vec{\Delta B}_E$
0° LONGITUDE
0° LATITUDE
θ
$\hat{z}$
LUNAR
EQUATOR
$\hat{y}$
$\hat{\phi}$
$\hat{\theta}$
$\hat{r}=\hat{x}$
APOLLO 12
SITE
$\hat{z}$ $\hat{\phi}$
ψ
$\hat{y}$
$\hat{\theta}$
ψ

Figure 5.

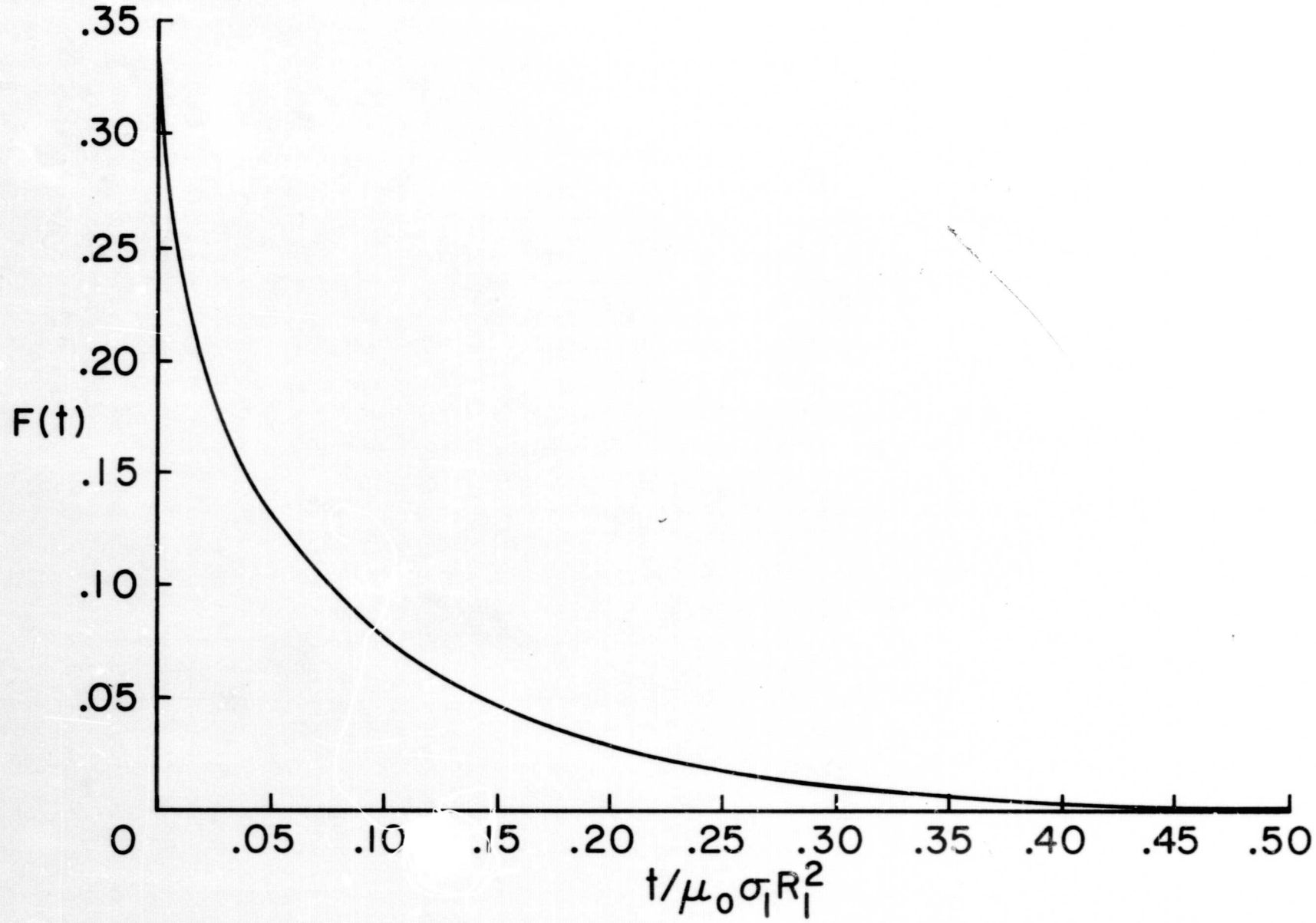
.35
.30
.25
.20
F(t)
.15
.10
.05
0
.05
.10
.15
.20
.25
.30
.35
.40
.45
.50
$t/\mu_0\sigma_1 R_1^2$

Figure 6.

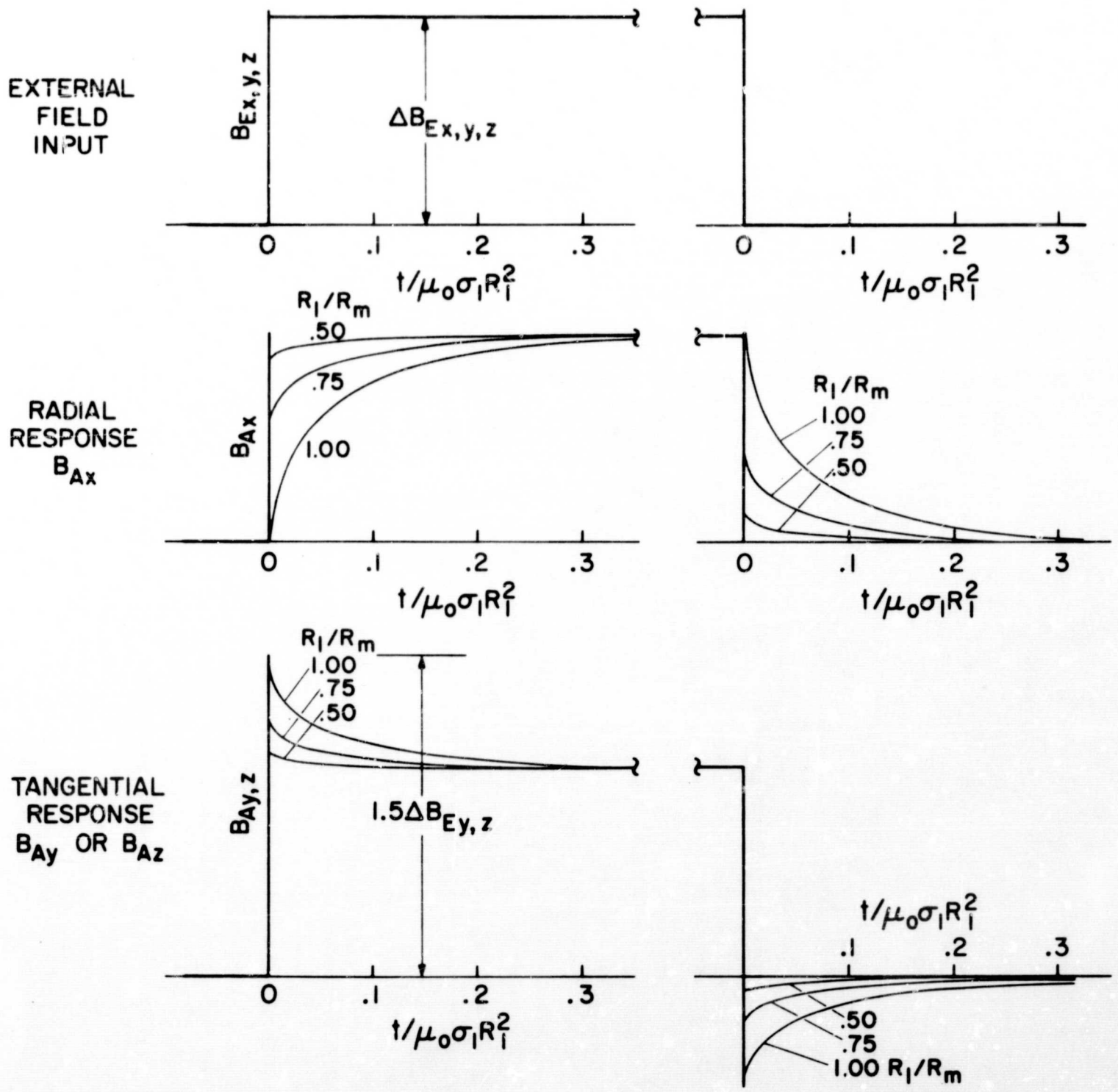
EXTERNAL FIELD INPUT
$B_{Ex,y,z}$
$\Delta B_{Ex,y,z}$
0
.1
.2
.3
$t/\mu_0\sigma_1 R_1^2$
RADIAL RESPONSE B_{Ax}
R_1/R_m
.50
.75
1.00
B_{Ax}
TANGENTIAL RESPONSE B_{Ay} OR B_{Az}
$B_{Ay,z}$
$1.5\Delta B_{Ey,z}$

Fig. 7

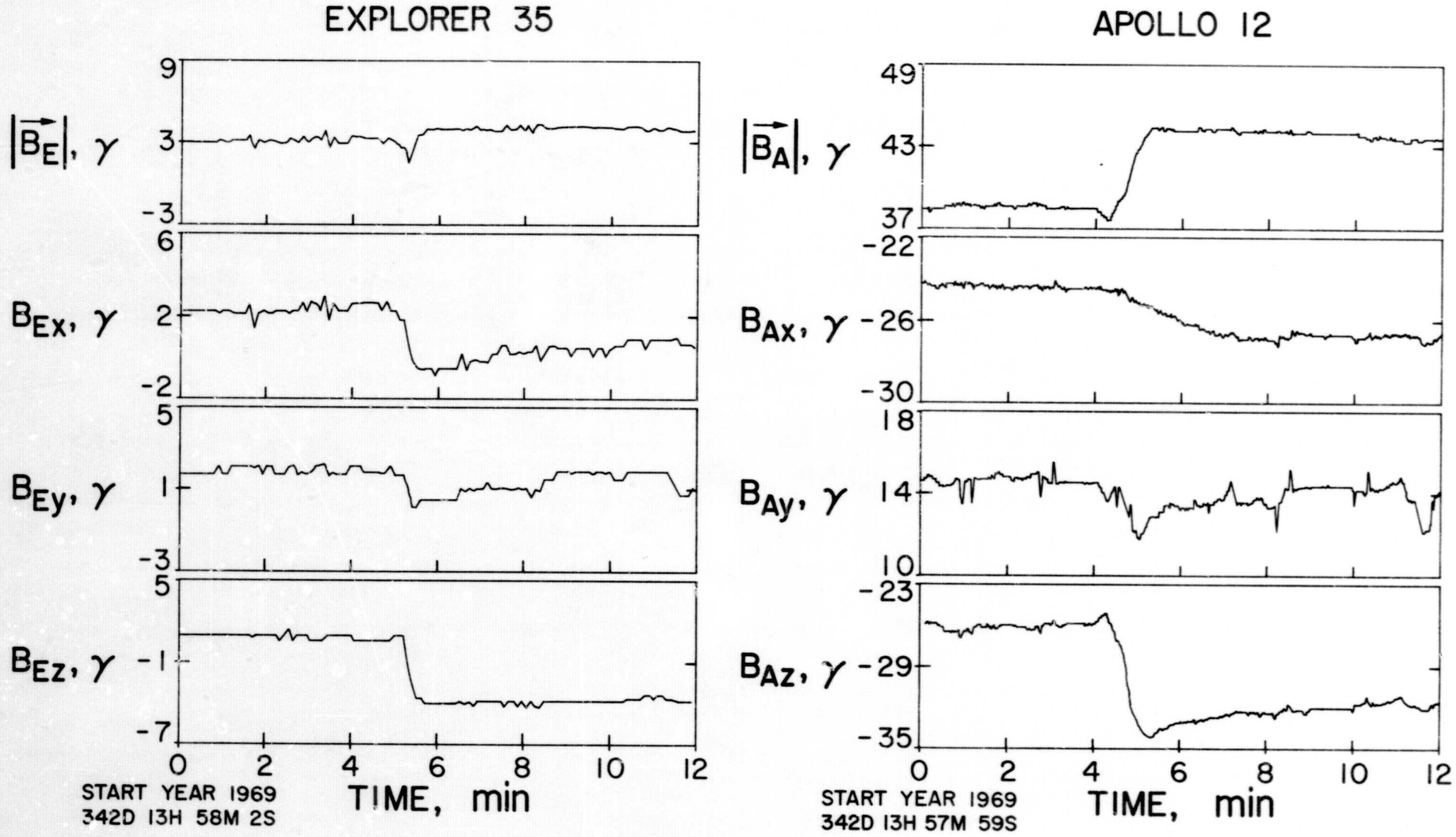
EXPLORER 35
APOLLO 12
$|\vec{B_E}|$, γ
B_{Ex}, γ
B_{Ey}, γ
B_{Ez}, γ
$|\vec{B_A}|$, γ
B_{Ax}, γ
B_{Ay}, γ
B_{Az}, γ
9
3
-3
6
2
-2
5
1
-3
5
-1
-7
49
43
37
-22
-26
-30
18
14
10
-23
-29
-35
0
2
4
6
8
10
12
TIME, min
START YEAR 1969
342D 13H 58M 2S
START YEAR 1969
342D 13H 57M 59S

Figure 8.

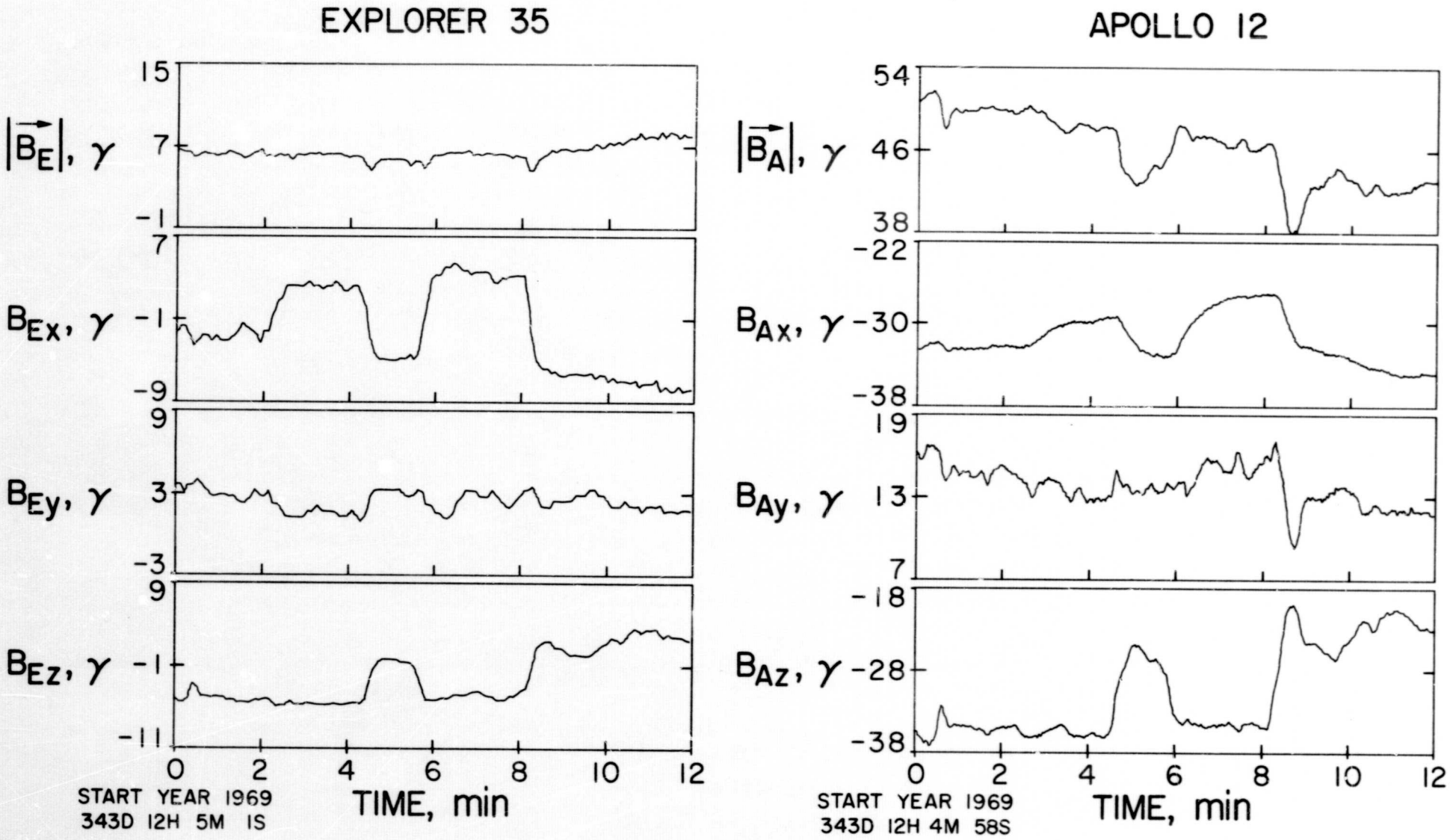
EXPLORER 35
APOLLO 12
$|\vec{B_E}|$, γ
B_{Ex}, γ
B_{Ey}, γ
B_{Ez}, γ
$|\vec{B_A}|$, γ
B_{Ax}, γ
B_{Ay}, γ
B_{Az}, γ
15
7
-1
7
-1
-9
9
3
-3
9
-1
-11
54
46
38
-22
-30
-38
19
13
7
-18
-28
-38
0
2
4
6
8
10
12
TIME, min
START YEAR 1969
343D 12H 5M 1S
START YEAR 1969
343D 12H 4M 58S

Figure 9.

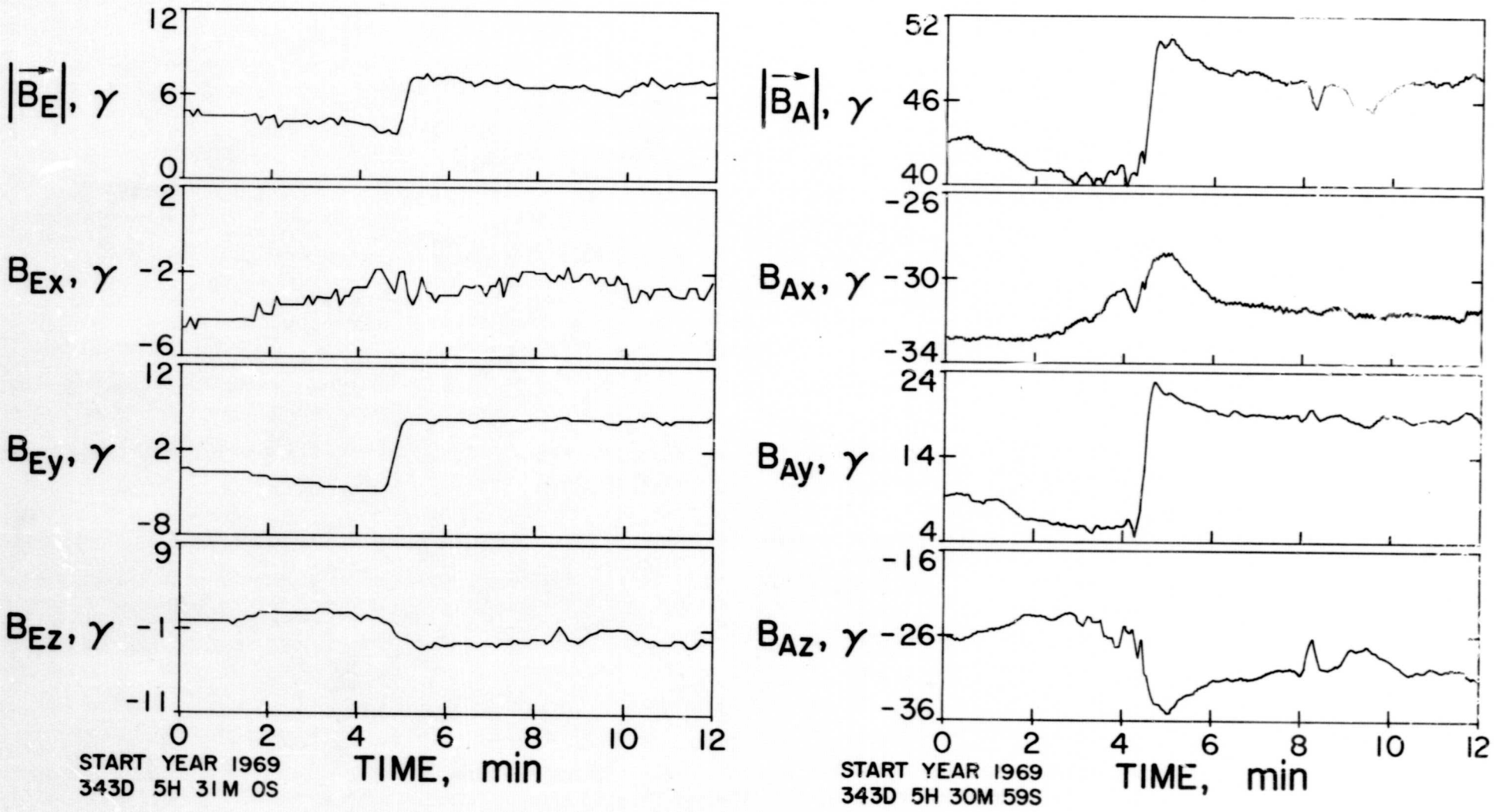
EXPLORER 35
$|\vec{B}_E|$, γ
12
6
0
B_{Ex}, γ
2
-2
-6
B_{Ey}, γ
12
2
-8
B_{Ez}, γ
9
-1
-11
0 2 4 6 8 10 12
START YEAR 1969
343D 5H 31M 0S
TIME, min
APOLLO 12
$|\vec{B}_A|$, γ
52
46
40
B_{Ax}, γ
-26
-30
-34
B_{Ay}, γ
24
14
4
B_{Az}, γ
-16
-26
-36
0 2 4 6 8 10 12
START YEAR 1969
343D 5H 30M 59S
TIME, min

Figure 10.

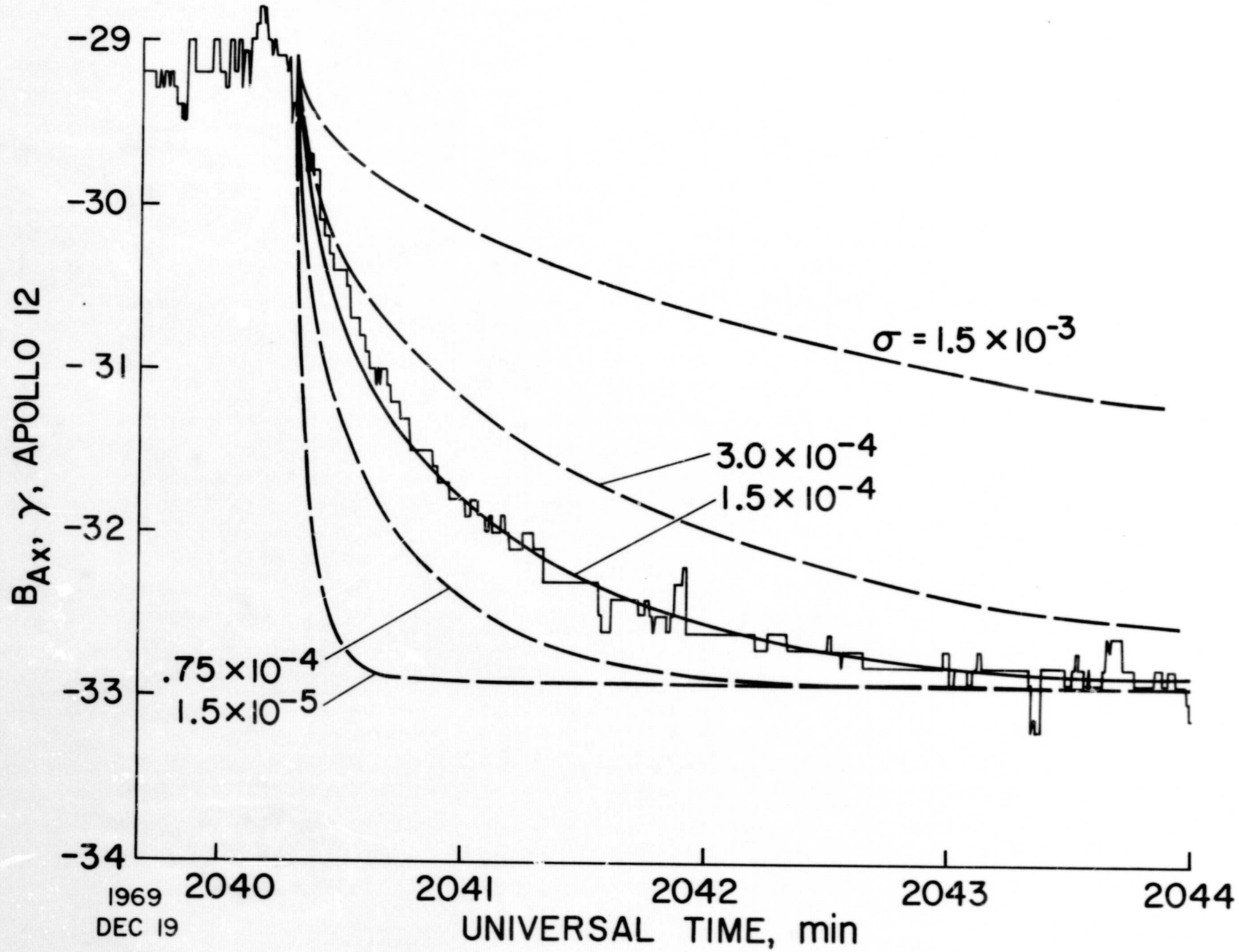
-29
-30
- 31
-32
-33
-34
B_{Ax}, γ, APOLLO 12
$\sigma = 1.5 \times 10^{-3}$
3.0×10^{-4}
1.5×10^{-4}
$.75 \times 10^{-4}$
1.5×10^{-5}
1969
DEC 19
2040
2041
2042
2043
2044
UNIVERSAL TIME, min

Figure 11.

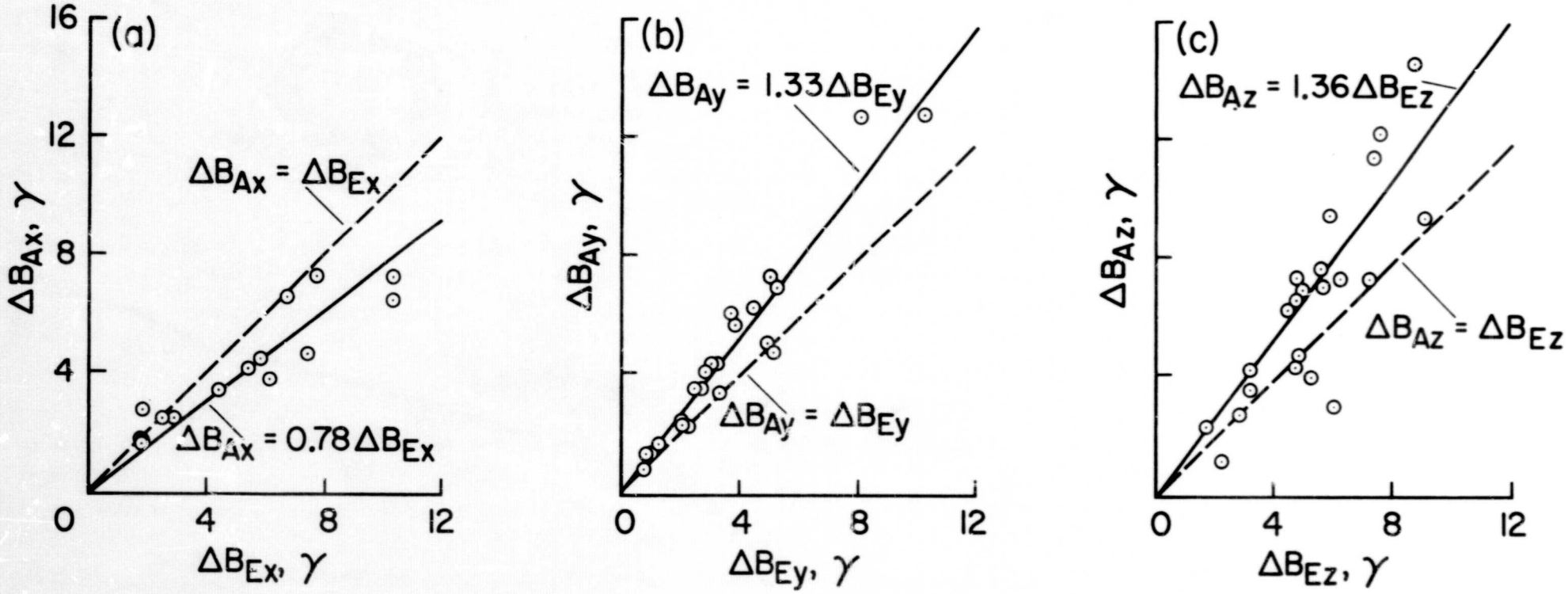
(a)
$\Delta B_{Ax} = \Delta B_{Ex}$
$\Delta B_{Ax} = 0.78\Delta B_{Ex}$
ΔB_{Ax}, γ
ΔB_{Ex}, γ
0
4
8
12
16
(b)
$\Delta B_{Ay} = 1.33\Delta B_{Ey}$
$\Delta B_{Ay} = \Delta B_{Ey}$
ΔB_{Ay}, γ
ΔB_{Ey}, γ
(c)
$\Delta B_{Az} = 1.36\Delta B_{Ez}$
$\Delta B_{Az} = \Delta B_{Ez}$
ΔB_{Az}, γ
ΔB_{Ez}, γ

Figure 12.

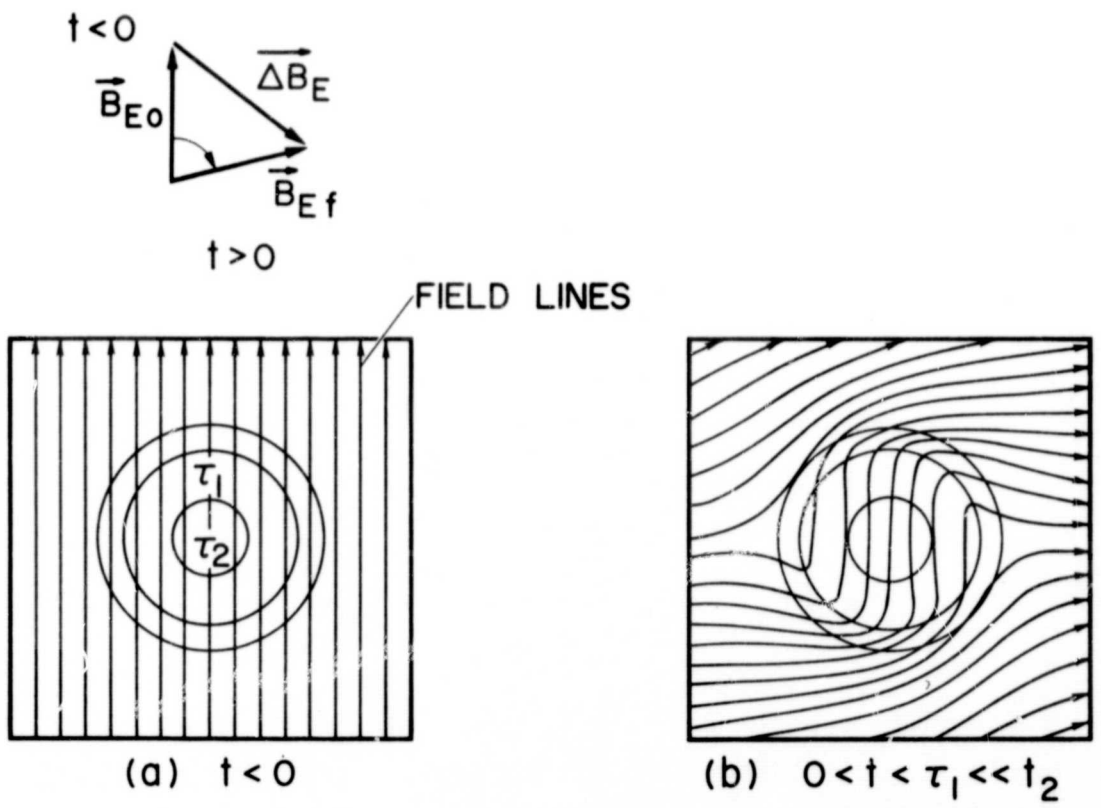
t<0
$\vec{B}_{Eo}$
$\vec{\Delta B}_E$
$\vec{B}_{Ef}$
t>0
FIELD LINES
τ_1
τ_2
(a) t<0
(b) $0<t<\tau_1<<t_2$
(c) $\tau_1<t<\tau_2$
(d) $t>>\tau_2$

Figure 13.

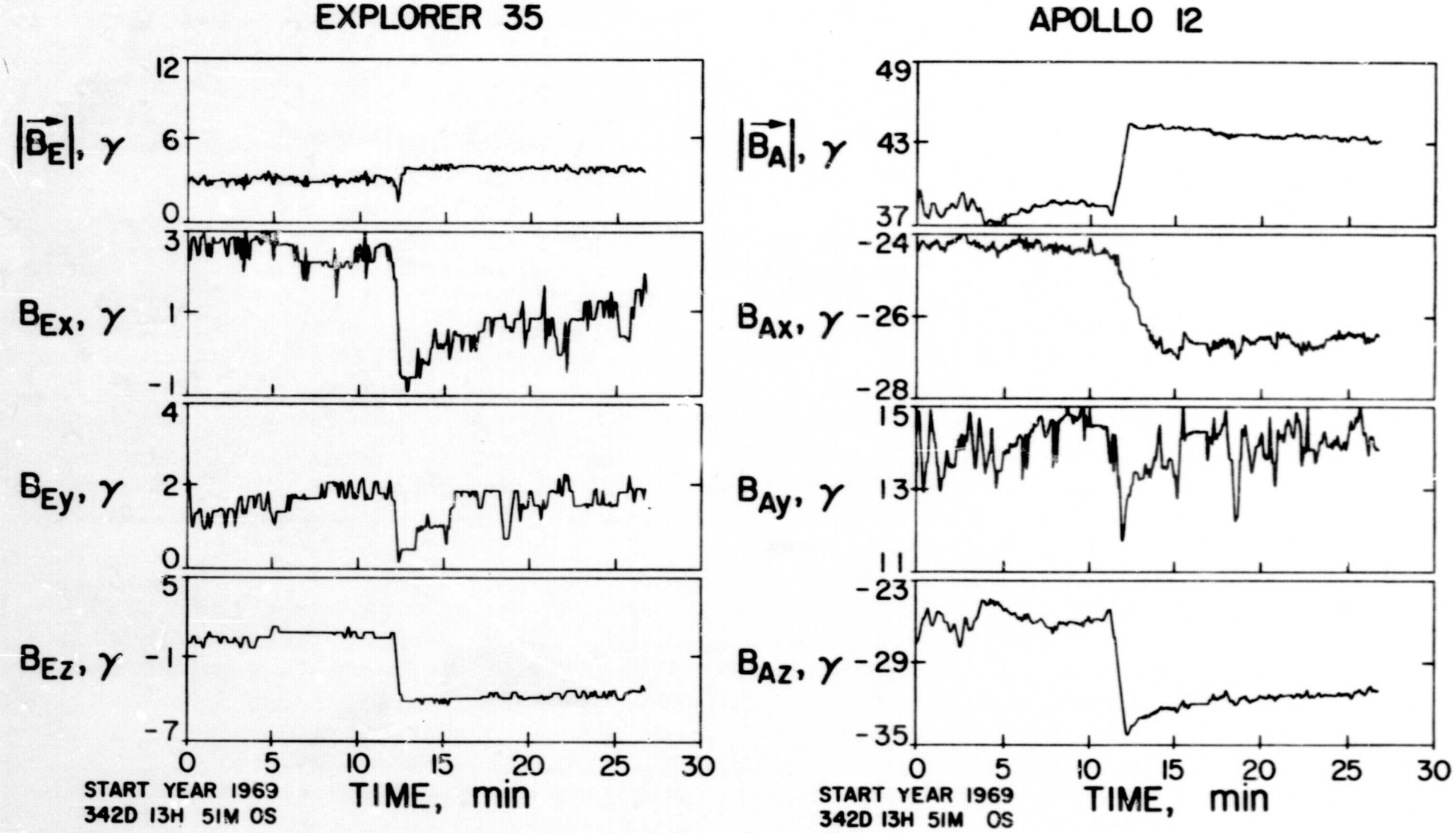
EXPLORER 35
APOLLO 12
$|\vec{B_E}|$, γ
B_{Ex}, γ
B_{Ey}, γ
B_{Ez}, γ
$|\vec{B_A}|$, γ
B_{Ax}, γ
B_{Ay}, γ
B_{Az}, γ
12
6
0
3
1
-1
4
2
0
5
-1
-7
49
43
37
-24
-26
-28
15
13
11
-23
-29
-35
0
5
10
15
20
25
30
START YEAR 1969
342D 13H 51M 0S
TIME, min

Fig. 14(a)

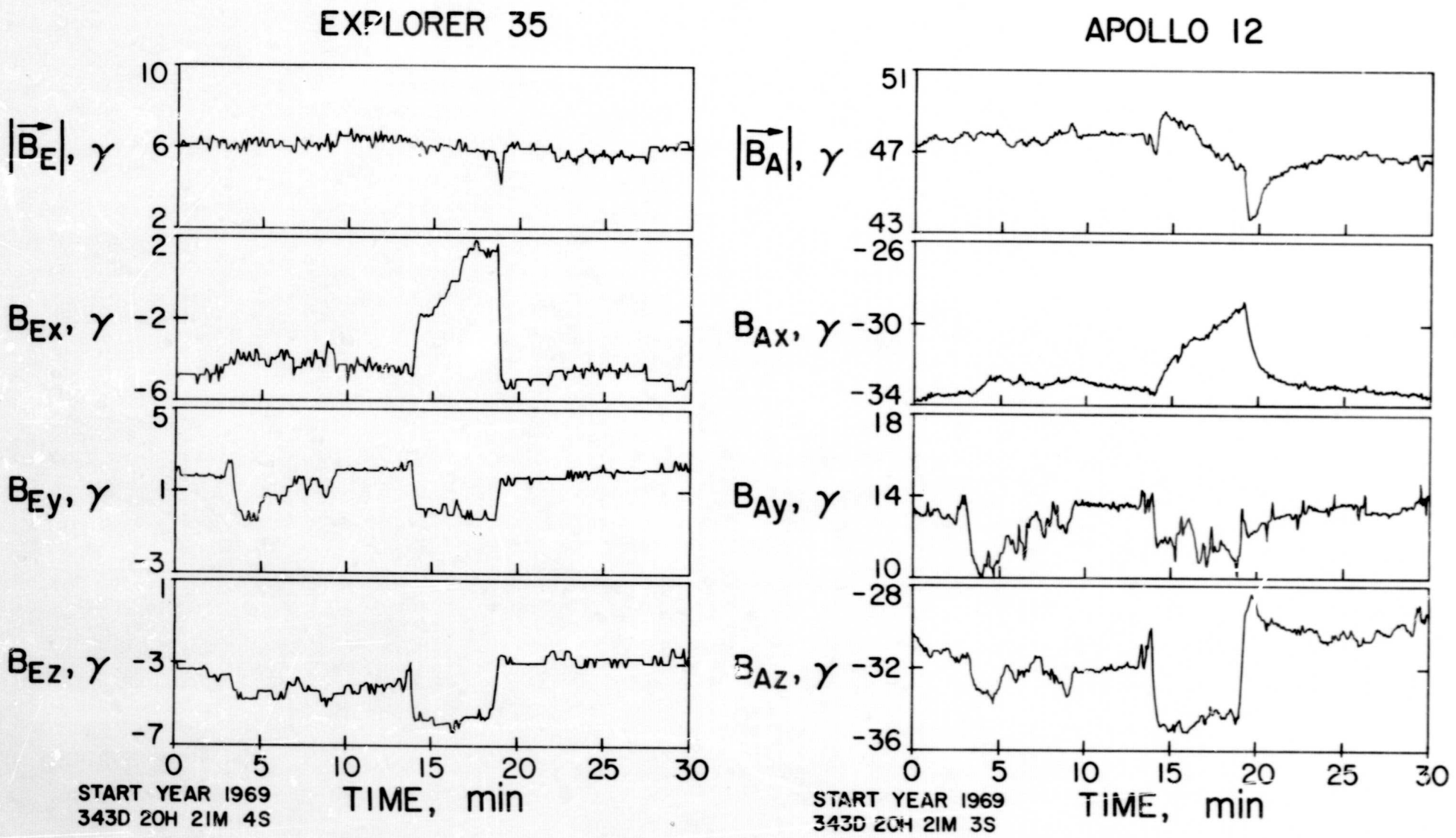
EXPLORER 35
APOLLO 12
$|\vec{B}_E|$, γ
B_{Ex}, γ
B_{Ey}, γ
B_{Ez}, γ
$|\vec{B}_A|$, γ
B_{Ax}, γ
B_{Ay}, γ
B_{Az}, γ
10
6
2
2
-2
-6
5
1
-3
1
-3
-7
51
47
43
-26
-30
-34
18
14
10
-28
-32
-36
0
5
10
15
20
25
30
START YEAR 1969
343D 20H 21M 4S
START YEAR 1969
343D 20H 21M 3S
TIME, min
TIME, min

Figure 14(b).

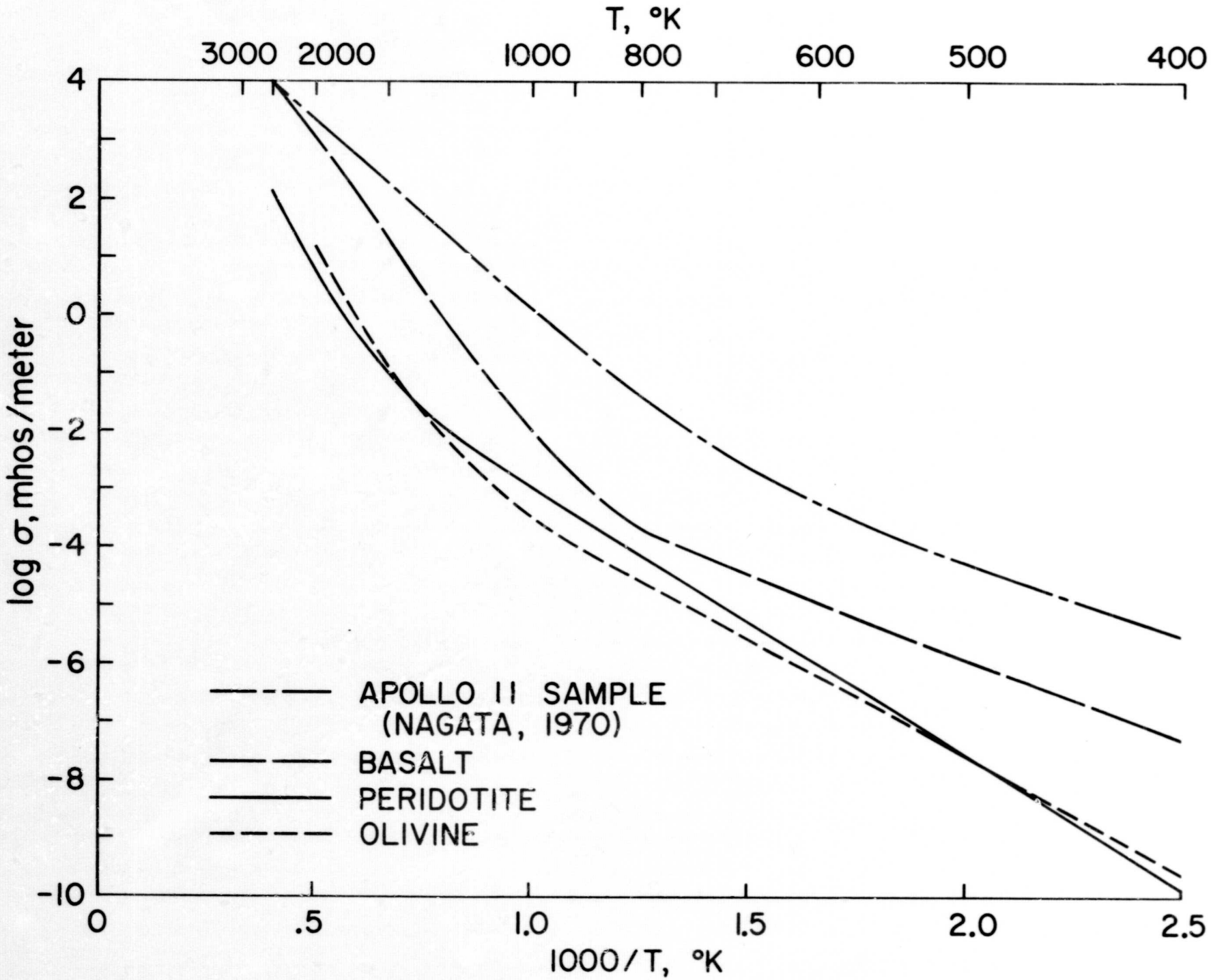
T, °K
3000
2000
1000
800
600
500
400
4
2
0
-2
-4
-6
-8
-10
log σ, mhos/meter
0
.5
1.0
1.5
2.0
2.5
1000/T, °K
APOLLO 11 SAMPLE
(NAGATA, 1970)
BASALT
PERIDOTITE
OLIVINE

Figure 15.

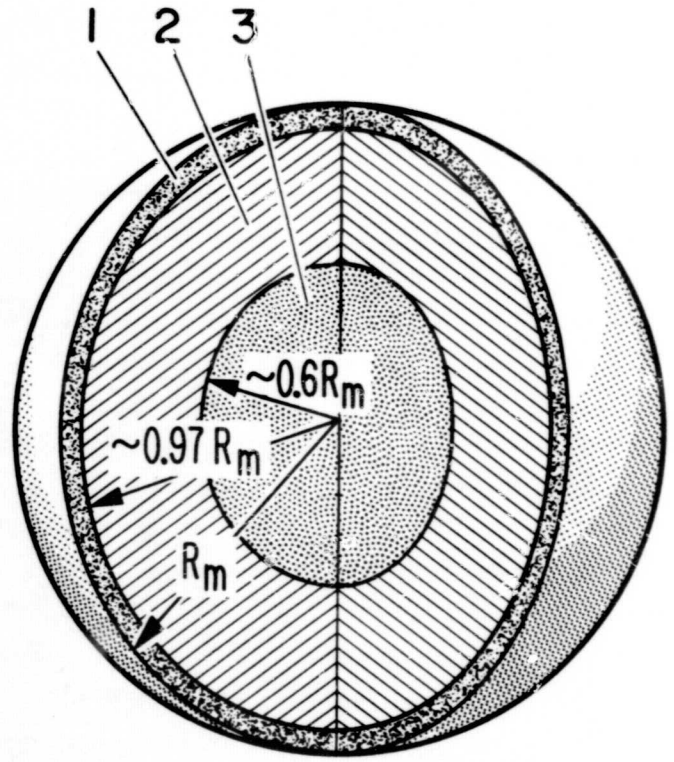

REGION	ELECTRICAL CONDUCTIVITY, σ, mhos/meter	TEMPERATURE, °K			
		OLIVINE	PERIDOTITE	BASALT	APOLLO 11 SURFACE SAMPLE
1	$<10^{-7}$	<530	<540	<420	<330
2	1.7×10^{-4}	840	940	790	550
3	$\gtrsim 10^{-2}$	≳1240	≳1270	≳1010	≳740

Figure 16.